ICARUS 104, 167–184 (1993)

Multiple Scattering of Light in a Spherical Cometary Atmosphere with an Axisymmetric Dust Jet

II. Image Simulation

KENNETH M. CHICK[1] AND TAMAS I. GOMBOSI

Department of Atmospheric and Space Sciences, and Space Physics Research Laboratory, University of Michigan, Ann Arbor, Michigan 48109

Received December 7, 1992; revised March 1, 1993

A numerical solution for the multiple scattering of light in spherical axisymmetric geometry is used to simulate observations of a model comet atmosphere as it would be seen by a near-flying satellite or by general wide-angle imaging techniques that might resolve the nucleus. We consider a spherically symmetric dust distribution, an axisymmetric dust jet, and a hollow cone of dust about the subsolar point. We calculate the specific intensity of both single- and multiply scattered light. Nucleus visibility and overall coma appearance is examined for varying phase angle. The appearance of the hollow cone is found to be especially sensitive to viewing geometry; at a phase angle of 90° it bears a strong resemblance to the "northern area of activity" observed by Giotto at Comet Halley. We also calculate the azimuth-integrated intensity, used by Thomas and Keller (1990, *Ann. Geophys.* 8, 147–166), as a measure of particle fragmentation Halley's coma, and examine the extent to which line-of-sight attenuation depletes the azimuth-integrated intensity near the nucleus, and multiple scattering enhances it.

1. INTRODUCTION

High-resolution imaging techniques have begun to reveal details of the inner comas of comets. Observations of various comets show structures in the dust–gas outflow of the inner coma, and images of the near-nucleus environment of Comet Halley have provided details on the nucleus itself and its jet-like emission of dust. We note, in particular, several outstanding properties of Halley which were evident in images taken by the Giotto Halley Multicolour Camera (HMC). First, for the period of the encounter, the images indicated that dust–gas emission was concentrated in a few collimated, sunward-facing jets. There was apparently negligible dust and gas emission from the shadowed side of the nucleus (Huebner *et al.* 1986, Keller and Thomas 1989), and the same major surface emission sources may have been active in Halley's 1910 apparition (Sekanina 1990). Second, within 100 km of the surface, the radial profile of the observed intensity was flatter than the ρ^{-1} dependence expected for constant-velocity radial outflow (where ρ is the line-of-sight impact parameter, essentially equal to the radial distance from the comet center in the image plane; Thomas and Keller 1987). It has been argued this is indicative of particle fragmentation in the outflowing dust (Szegö *et al.* 1988, Thomas and Keller 1990). Third, despite the fact that dust emission was concentrated on the sunward face of the nucleus, the overall coma appeared quite homogeneous, with a ratio of scattered light intensity integrated over the sunward hemisphere to the intensity integrated over the antisunward hemisphere of only 3.2 : 1 (Keller and Thomas 1989). One explanation for this homogeneity may be near-nucleus breezes blowing dust tangentially to the antisunward portion of the coma (Keller *et al.* 1990). These near-surface breezes may represent a means of feedback between the discrete jet sources and the rest of the inactive surface (Sekanina 1990). In order to interpret such results, and relate them to models of dust–gas flow in the inner coma, it is essential to be able to simulate images of the coma.

The earliest work on simulation of near-nucleus images was by Hellmich and Keller (1981) in preparation for the Giotto fly-by. They modeled single-scattered light in a spherically symmetric dust coma and allowed for considerable surface reflection. They calculated relations between coma optical depth and nucleus visibility and defined a contrast function quantifying the brightness of the nucleus relative to its surrounding coma. Halley's nucleus proved to be relatively clear in HMC images, except at the base of the sunward dust emission region,

[1] Present address: NASA Ames Research Center, MS 245-3, Moffett Field, CA 94035.

0019-1035/93 $5.00

corresponding to a line of sight through the optically deepest portion of the coma; and the nucleus appeared very unreflective. Hellmich and Keller's results implicity predicted a steepening of the intensity profile with respect to the line-of-sight impact parameter ρ near the nucleus, due to acceleration of the dust. In the actual HMC observations, any acceleration effects steepening the intensity profile near the nucleus were overwhelmed by flattening effects, in particular by particle fragmentation.

Huebner *et al.* (1988) focused on an explanation for the deviations in the observed Giotto HMC intensity profiles from the ρ^{-1} dependence expected for uniform ejection of dust over the nucleus surface, with constant-velocity radial flow. They showed that overlapping cones of dust emission at the surface could account for the observed deviation. They modeled nucleus emission as originating at several separated point sources on the surface, with each point source emitting into a cone. Far from the nucleus all the cones overlap, and appear as if they resulted from a single point source of approximately radial outflow. As the line of sight approaches the nucleus it fails to intersect all the cones, leading to a flattening of the profile due to a relative depletion in the dust column density near the nucleus.

Thomas and Keller (1990) used the azimuth-integrated intensity in HMC images to infer the surface integral of dust over a closed volume surrounding the nucleus, which by Gauss' Law measures the sources enclosed in the volume. The behavior of the azimuth-integrated intensity in function of ρ indicates that an increasing Gaussian volume encloses an increasing source, and they argue that particle fragmentation in the outflow accounts for the extra source. Thomas and Keller (1991) have also compared HMC observations with measurements by other Giotto instruments and placed constraints on the optical properties of the dust, the total dust production rate, and the dust-to-gas ratio. They estimated a maximum observed optical depth of about 0.4, measured transverse through the brightest jet.

The appearance of the jets was investigated by Reitsema *et al.* (1989), who found the Giotto HMC coma images could be well fit with three jets of Gaussian angular cross section, and that about 26% of the coma brightness was due to an unstructured dust background. They used the dust jet distribution as a diagnostic of collimation and lateral dispersion of outflow. Kitamura (1986) modeled a hydrodynamic, time-dependent axisymmetric dust–gas jet and found that the jet develops a hollow cone structure. Körösmezey and Gombosi (1990) used a dust–gas hydrodynamic model to establish to relation between jet strength and opening angle and explore related jet variation with respect to time. They found the jet structure varied with the amount of dust production, and that a subsolar dust spike forms if there is sufficiently strong emission. Kitamura (1990) modeled the interaction between two jets, determining shock formation between the colliding jets, and he speculated on optical signatures of the shock waves in scattered light from the dust.

Quite recently, Weaver *et al.* (1992) have used the Hubble Space Telescope (HST) to record high spatial resolution images of Comet Levy 1990c. The resolution is much lower than that of the Giotto HMC: pixel size is about 78 km in the image plane, so the nucleus is not resolved, but the images reveal details of the inner coma and its evolution in time. Two sets of photographs taken 6.5 hr apart show an arc of dust propagating outward through the sunward portion of the coma. There was a broad, approximately axisymmetric, sunward dust emission feature; and the radial intensity profile followed the ρ^{-1} law.

On greater length scales, dust is blown antisunward by radiation pressure, and comas are approximately paraboloids about the nucleus (the fountain model). Eddington (1910) discussed qualitatively the coma appearance on this scale. Isophote patterns for fountain models have been studied by Mokhnach (1938, 1958a,b), and Wallace and Miller (1958): for isotropic constant-speed emission, the density integrated along the line-of-sight varies as ρ^{-1}, and the intensity follows this profile, just as for the spherically symmetric coma discussed above. More recently Sekanina (1987) has developed an elaborate numerical model which simulates large scale coma images for dust emission from a rotating nucleus. On this scale, light scattering can be treated with great simplifications over our work, but Sekanina has demonstrated the utility of coma image simulation for understanding nucleus emission.

In addition to radiation intensity, measurement of optical polarization has proven to be a tracer for coma dust properties. Using Q and U to denote the linear polarization parameters, and V the circular polarization parameter, the degree of polarization, $(U^2 + Q^2 + V^2)^{1/2}/I$, is scaled to eliminate sharp gradients present in the intensity (Eaton *et al.* 1991). Detailed intensity and polarization maps of the near-nucleus region ($r < 3400$ km) of Comet Levy 1990c have been made by Renard *et al.* (1992). In accord with earlier studies (Dollfus and Suchail 1987, Eaton *et al.* 1988) they find polarization varies when jets are present, with polarization a maximum in the jet at 500–1000 km from the nucleus. Renard *et al.* interpret these results as showing the physical properties of the dust change during outflow. Sen *et al.* (1990) suggest a lack of polarization observed near Halley's nucleus may be due to multiple scattering effects of fresh dust ejecta. Metz and Haefner (1987) also suggest that multiple scattering prevailed near the nucleus during their March 1986 observations of circular polarization at Comet Halley.

To date, light-scattering effects related to wide-angle

coma imaging have been discussed only in qualitative, or approximate terms. Most image analysis considers only single-scattered light, and often neglects line-of-sight attenuation. Line-of-sight attenuation will deplete the observed intensity, especially near the nucleus where the greatest optical depths occur. Multiple scattering of light will enhance the intensity, again preferentially near the nucleus, acting as a "source" in the Gaussian volume considered by Thomas and Keller; it may also brighten jet features. Multiple scattering may explain the observed depletion in polarization near the nucleus during outbursts and in the presence of jets. So far no one has quantified multiple scattering in image interpretation. Both line-of-sight attenuation and multiple scattering will depend strongly on viewing geometry.

In order to model coma radiative transfer we have developed a multidimensional numerical successive approximation solution for the multiple scattering of light in an axisymmetric atmosphere (Chick and Gombosi 1992, hereafter Paper I). We apply it here to the simulation of images taken by a near-flying satellite such as Giotto or by general wide-angle imaging techniques. The calculations provide insight into light scattering and viewing geometry effects in the imaging of comets. They will also provide a tool to relate flow patterns from dust–gas hydrodynamic modeling of comas to observations (for samples of such modeling see Gombosi *et al.* 1986, Kitamura 1986, 1990, Körösmezy and Gombosi 1990, Konno *et al.* 1992).

2. THE MODEL FOR LIGHT SCATTERING

The numerical successive approximation solution for the multiple scattering of light has already been described in Paper I; we summarize briefly the outstanding features and the details unique to the image simulation. The coma is assumed to be a spherical shell of radius $r_{\max}$, centered about a spherical nucleus of radius R. We have taken the nucleus' albedo to be zero, which should be a good approximation (see for example Keller *et al.* 1987). The model coma and the coordinate system are shown in Fig. 1; position is $\mathbf{r}(r, \theta)$; direction is $\mathbf{\Omega}(\Theta', \Phi')$, where Θ' and Φ' are the direction angle and azimuth, respectively, in the spherical reference at $\mathbf{r}$. For consistency with Paper I we have denoted the direction coordinates in this reference with a prime. Due to axisymmetry, the position azimuth, ϕ, never appears explicitly in the solution. Parallel solar rays are incident from the direction $\mathbf{\Omega}_0 = -\mathbf{e}_z$ in Fig. 1, described by $I(r_{\max}, \theta, \mathbf{\Omega}) = \pi S \delta_2(\mathbf{\Omega} \cdot \mathbf{\Omega}_0)$ for θ such that $\mathbf{\Omega}_0 \cdot \mathbf{e}_r < 0$, where δ_2 is a two-dimensional delta function and S is the solar constant. We simulate both a spherically symmetric coma and a coma with a sunward, axisymmetric dust distribution at the subsolar point.

In the absence of external forces, constant isotropic dust ejection from a point source (or constant radial outflow uniformly over the nucleus surface) yields a spherically symmetric coma, with an extinction coefficient

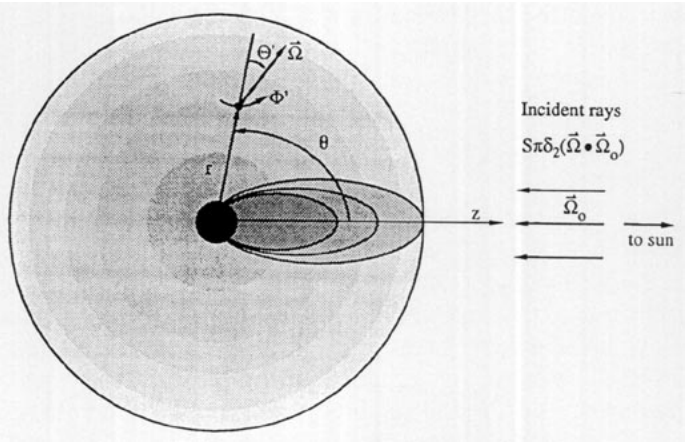

FIG. 1. The model coma and coordinate system. Position is $\mathbf{r}(r, \theta)$, and direction is $\mathbf{\Omega}(\Theta', \Phi')$ in the spherical reference at $\mathbf{r}$.

$$\alpha(r) = \frac{R\tau_0}{r^2}. \tag{1}$$

The extinction coefficient is related to the dust cross section for scattering and absorption, σ, and the number density of dust, n, by $\alpha = n\sigma$. We assume the cross section σ is constant throughout the coma. The characteristic optical depth in the radial direction from the surface to infinity is τ_0. The r^{-2} form follows either from the analysis of Mokhnach (1958b), or by invoking the continuity equation.

To simulate a coma with an axisymmetric dust jet, the extinction coefficient is parameterized as

$$\alpha(r, \theta) = \frac{R\tau_0}{r^2}\,[(X - 1)\exp(-\theta^2/W^2) + 1], \tag{2}$$

where θ is position angle measured off the subsolar point, X is the jet strength, and W is the angular width (Kitamura 1986). This parameterization superposes a Gaussian cross section jet over a spherically symmetric background, of characteristic depth τ_0. For comparison to the work of Thomas and Keller (1990), we note that this parameterization is consistent with a constant radial outflow of dust over the nucleus surface at $r = R$, with variation in source strength, Q, with angle off the subsolar point. This can be seen by assuming constant radial flow, and considering the continuity equation

$$\nabla \cdot n\mathbf{v} = \frac{\nu}{r^2}\frac{\partial}{\partial r}(r^2 n(r, \theta)) = Q(\theta)\delta(r - R), \tag{3}$$

where v is the radial speed, and Q is measured in particles sec^{-1} area^{-1}. Integrating with respect to r,

$$n(r, \theta) = \frac{R^2 Q(\theta)}{v r^2}. \quad (4)$$

If we convert the number density to an extinction coefficient as in Paper I, we arrive at Eq. (2).

Reitsema *et al.* (1989) noted that the width W should be sensitive to the dust size distribution and to tangential gas flow out of the jet; large particles should be concentrated in the center of the jet, smaller particles in the wings. Reitsema *et al.* found the jets observed by Giotto HMC were well-fit by Gaussian cross sections, $W \approx 50°$–$85°$ (although they consider a cone of dust emission with its vertex at the surface). Hubble Space Telescope images of Comet Levy 1990c also indicate this axisymmetric Gaussian parameterization is realistic, with $W \approx 135°$ (Weaver *et al.* 1992). We also simulate a hollow cone of emission at the subsolar point by replacing θ in Eq. (2) with $\theta - \theta_c$, where θ_c is the opening angle of the cone edge.

The specific intensity of light is

$$I(\mathbf{r}, \boldsymbol{\Omega}) = S\pi\delta_2(\boldsymbol{\Omega} \cdot \boldsymbol{\Omega}_0) e^{-\int_0^{s_b(\mathbf{r}, \boldsymbol{\Omega}_0)} \alpha(\mathbf{r} - s\boldsymbol{\Omega}_0)\, ds} + \int_0^{s_b(\mathbf{r}, \boldsymbol{\Omega})} ds\, e^{-\int_0^s \alpha(\mathbf{r} - s'\boldsymbol{\Omega})\, ds'} \frac{\alpha(\mathbf{r} - s\boldsymbol{\Omega})\lambda}{4\pi} \int_{4\pi} d\boldsymbol{\Omega}' P(\boldsymbol{\Omega} \cdot \boldsymbol{\Omega}') I(\mathbf{r} - s\boldsymbol{\Omega}, \boldsymbol{\Omega}'), \quad (5)$$

where λ is the single-scatter albedo; P is the phase function, parameterized by the Henyey–Greenstein function (see Paper I), where g is a parameter ($0 \le g < 1$) characterizing the forward peaking of the phase function with scattering angle, $g = 0$ is isotropic scattering, and $g \to 1$ is complete forward scattering. The path length from position $\mathbf{r}$ to the boundary of the domain in direction $-\boldsymbol{\Omega}$ is $s_b(\mathbf{r}, \boldsymbol{\Omega})$; an explicit formula is given in Paper I. The parameters λ, P, and α are taken to represent an average over dust size distribution and wavelength of light; λ and P are assumed to be constant throughout the coma. To solve for the specific intensity, we discretize in position and define discrete ordinates in direction. $I(\mathbf{r}, \boldsymbol{\Omega})$ is decomposed into unscattered light, I_0, single scattered light, I_1, and light scattered two or more times, $I_{\ge 2}$. The unscattered and single scattered light is found by numerical evaluation of analytic solutions. Light scattered two or more times is determined by successive approximation ("lambda iteration") to an equation in the form of Eq. (5).

To construct an image for an arbitrary viewing position external to the coma, we must interpolate values of the specific intensity of diffuse light emerging from the atmosphere. The computed values are available at positions

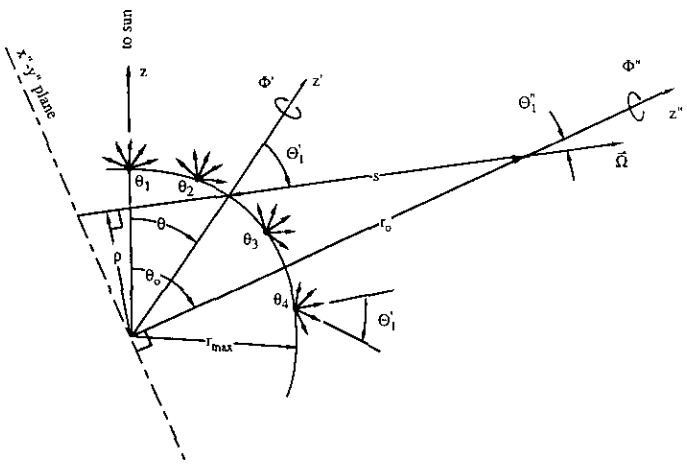

FIG. 2. To construct an image, we interpolate the computed specific intensity emerging at the top of the coma.

$\{(r_{\max}, \theta_k): k = 1, K\}$ in directions $\{(\Theta_i', \Phi_j'): i = 1, N; j = 1, M\}$. Referring to Fig. 2, for each $\Theta_i' < \pi/2$ we scan through observation azimuth Φ'' at arbitrary values, $0 < \Phi'' < \pi$. At each value of Φ'', we determine the position angle of emission θ, and the direction azimuth Φ'. A single point in a simulated image is thus $I(r_{\max}, \theta, \Theta_i', \Phi')$, and is found by interpolating the numerical solution on the θ-angle grid, and interpolating in direction azimuth, Φ'. Details on the computation are given in Appendix A.

3. IMAGE SIMULATION RESULTS

We present simulated observations of the total diffuse specific intensity, $I_1 + I_{\ge 2}$, for an observer located at a distance $r_0 = 1000$ comet radii from the center of the comet, for varying Sun–comet–observer phase angle, θ_0. The false-color plots are intended to show the qualitative bright and dark features of the image; the reddish color was included only to enhance the appearance. Incident solar rays arrive from the left in the diagrams. The nucleus is at the center of each diagram and has unit radius. For each phase angle, we also show the corresponding cross sections of the specific intensity along the $y'' = 0$ (Sun–comet) axis of the images. The total diffuse specific intensity is shown in solid circles at each discrete direction angle Θ_i' in the cross section, and the corresponding single scattered component, I_1, is shown with an open circle.

There is a discontinuity in the image when the line of sight is tangent to the nucleus. This discontinuity was noted by Hellmich and Keller (1981; see their Fig. 5 for $\tau_0 = 0.6$). In general high-curvature effects appear in the solution near this discontinuity, and many discrete ordinates are required to accurately resolve the abrupt curvature. The discrete ordinate scheme concentrates several

ordinates with lines-of-sight just off the limb in the high curvature region, a few ordinates with lines-of-sight into the nucleus, and the rest distributed over the "open sky." We have used an azimuthal quadrature order of 7 for these diagrams, with azimuth ordinates Φ_j' concentrated on the sunward half of the image. The left (sunward) portion of the cross section plots corresponds to $\Phi_M' = \pi$, and the right (antisunward) portion to $\Phi_1' = 0$.

To determine sufficient discrete ordinate resolution we gradually increased the quadrature order until all limb curvature effects appeared to be resolved in single-scattered images, and used these ordinates for the $I_{\geq 2}$ iteration. This approach is not completely satisfactory because curvature and slope increase in the $I_{\geq 2}$ iteration, but do not appear to change the result significantly. At worst, it appears that in some cases we cannot distinguish a jump discontinuity from a very sharp but continuous fall-off in intensity across the nucleus' limb, or a continuous cusp at the limb.

3a. Simulated Images of a Spherically Symmetric Coma

We first show simulated images for a spherically symmetric coma. Figure 3 is for a coma of characteristic optical depth $\tau_0 = 0.5$, and Fig. 4 is for $\tau_0 = 3$. For calculation of $I_{\geq 2}$ the coma was truncated at $r_{max} = 35$ comet radii for $\tau_0 = 0.5$, and the code was run for five iterations. For the case $\tau_0 = 3$ the coma was truncated at $r_{max} = 100$ comet radii, and the code was run for 11 iterations. Optical properties for Figs. 3 and 4 are chosen to maximize all scattering effects. The single scatter albedo is $\lambda = 1$, which puts an upper limit on multiple scattering effects. The Henyey–Greenstein phase function parameter is $g = 0$, corresponding to isotropic scattering. This also maximizes scattering effects, since forward-scattering will tend to transport light directly through the coma with less spatial or directional redistribution. In Figs. 5 and 6 we investigate the effect of forward-scattering.

In Fig. 3a the phase angle is $\theta_0 = 0°$, opposition, so the Sun is directly behind the observer and we see backscattered light. "Isophotes" are circular about the nucleus. The nucleus appears as a dark disk in the center of the image. The light arriving from just off the limb is the brightest portion of the image due to a maximum number of scattering sites along the line-of-sight, an exaggerated limb brightening effect. Referring to the $y'' = 0$ cross section for this image, we see this effect is accentuated in the multiply scattered component, $I_{\geq 2}$. As the line of sight passes from the limb to the center of the nucleus the signal is increasingly depleted since the decreasing optical depth supplies fewer and fewer scattering-sites.

In Fig. 3b the phase angle is $\theta_0 = 45°$. A bright crescent of light forms on the sunward (left) side of the image. The radiation field changes abruptly across both the sunward and antisunward limbs. This variation is sharpened in the multiply scattered components. The antisunward nucleus edge, especially, is just barely resolvable in the single scattered field, but appears as a strong discontinuity in the multiply scattered light.

Figure 3c demonstrates the simulated image at phase angle $\theta_0 = 135°$. Again there is a bright crescent on the sunward limb of the nucleus which peaks before the limb, and drops sharply across it. The nucleus appears relatively darker than its surroundings compared to Fig. 3b because it blocks some sunlight. The shadow swept out by the nucleus is apparent in the antisunward portion of the coma in the false-color plot.

The cross section plot for $\theta_0 = 135°$, Fig. 3c, shows that the antisunward limb is resolvable as sharp trough in the intensity. There is a peak of scattered light distinctly beyond the antisunward limb. This is explained by noting that the dust scattering sites act both as a source of scattered light and as a line-of-sight attenuation, and as the line-of-sight's tangent point approaches the limb, the concentration of scattering sites increases. As the line-of-sight approaches the nucleus through shallow optical depths to within about 2 comet radii off the antisunward limb, the net effect is to sample an increasing "signal", so the image brightens. Within 2 comet radii the optical depth becomes deep enough that the net effect is attenuation, and the image is increasingly dimmed. This effect may be present in Keller and Thomas' (1989) analysis of the antisunward limb of Halley (see their Fig. 2).

Figure 3d shows the simulated image for phase angle $\theta_0 = 180°$, with the comet nucleus eclipsing the Sun. The single-scattered component shown in Fig. 3d is discontinuous across the limb, dropping to zero behind the nucleus, but the multiply scattered component $I_{\geq 2}$ fills in the gap. The brightness peaks distinctly beyond the limb, again showing that as the line-of-sight optical depth increases there is a trade-off between the role played by the scattering sites as sources and as attenuation. Also, this brightness peak is again sharpened in the multiply scattered component.

Figure 4a shows a spherically symmetric coma, $\tau_0 = 3$, viewed at opposition, phase angle $\theta_0 = 0°$. The top cross section shows the whole domain and the lower is a blow-up of the near-nucleus region. The jump in intensity across the limb is less dramatic than in Fig. 4a, and the nucleus is barely resolvable, due to obscuration by dust. The center of the image has an intensity peak: compared to Fig. 3a, optical depths are now large enough on both sides of the limb that line-of-sight attenuation dominates, and there is a slight trough in the intensity at the limb.

The peak in intensity in the center of the image is still apparent at $\theta_0 = 45°$ in Fig. 4b. The variation in I_1 is

almost smooth, but the multiply scattered component accentuates jumps across the limbs, so the nucleus can be resolved. The extent of the bright sunward crescent is increased over Fig. 3b. At $\theta_0 = 135°$, Fig. 4c, the nucleus is a dark disk silhouetted against the coma. A bright maximum forms distinctly to the left of the dark disk, whereas in Fig. 3c a bright crescent formed at the left disk edge.

At $\theta_0 = 180°$, Fig. 4d, the nucleus again eclipses the Sun. The antisunward shadow is illuminated purely by multiply scattered light, and the high dust density for this case allows light to "migrate" into the region after many scatterings. Scattered light fills in the antisunward shadow, and the shadow cast by the nucleus appears much brighter than in Fig. 3d. The total number of numerical iterations represents an average number of photon scatterings before emergence from the domain, therefore the solution converges very slowly in the antisunward shadow. Bright intensity peaks form well beyond the limb, with line-of-sight attenuation of incident sunlight the dominant effect in the long optical depths within 4 comet radii of the limb.

Micrometer-sized dust particles typical of comas should scatter light preferentially in the incident direction, so in Figs. 5 and 6 we compare images with isotropic scattering, $g = 0$, and forward-scattering, $g = 0.75$. The coma is spherically symmetric, of optical depth $\tau_0 = 1$. In Fig. 5 we compare $y'' = 0$ cross sections of simulated images at $\theta_0 = 45°$. At this phase angle light must be reversed from its incident direction through 135° in order to reach the observer; isotropic scattering does this more efficiently than forward-scattering, and thus gives a much brighter image. For $g = 0.75$, a larger fraction of the intensity is due to $I_{\geq 2}$, because in order for the light to be reversed in direction it must be scattered many times.

A forward-peaked phase function allows scattered light to follow its initial direction more closely, and light penetrates efficiently through the coma. In Fig. 6, we consider phase angle $\theta_0 = 135°$, where we observe light coming from near the incident direction; thus the image is much brighter for $g = 0.75$ than for $g = 0$. For $g = 0$ the multiply scattered intensity peaks beyond the sunward limb; the image is dimmed close to the limb where light is scattered out of the incident direction by the highest optical depths. For $g = 0.75$, the same optical depths at the limb present little attenuation, and intensity peaks at the limb.

We believe that our results for $g = 0.75$ are qualitatively correct, but it is difficult to be certain of the accuracy. The "triple-Gauss" quadrature scheme we use for direction angle Θ' (described in Paper I) allows us to resolve the abrupt variation in the intensity near the nucleus; however, it does not yield an accurate evaluation of the scattering integral in Eq. (5) when the phase function is strongly forward-peaked. This problem is discussed by Lewis and Miller (1984). Tests we have performed on our code indicate the results should be accurate for $g \leq 0.5$; more testing is needed for $g > 0.5$.

Thus comparing images of shallow and deep spherically symmetric comas under high scattering conditions shows the nature of multiple scattering around the nucleus, and the discontinuities that occur in the solution at the nucleus limb, extending the visibility study of Hellmich and Keller (1981). In the optically shallower case ($\tau_0 = 0.5$), bright crescents form at the limb of the nucleus, and there is an abrupt jump in intensity across the limb, so the dark nucleus edge is visible. Multiply scattered light tends to enhance the crescent that forms on the sunward edge of the nucleus and sharpen the silhouette of the antisunward edge.

The overall pattern of a dark disk with bright maxima just beyond the limb is in qualitative agreement with the isotropic scattering results of Adams and Kattawar (1978) and the forward-scattering results of Kattawar and Adams (1978), both based on a Monte Carlo approach. They plotted "radiance vs nadir angle" for a constant-density spherical shell atmosphere, $\tau_0 = 0.25$ and $\tau_0 = 1$, but with $r_{max} = 6471/6371 \approx 1.016$ earth radii. A discontinuity across the limb (or horizon) is not apparent in their plots; their model atmosphere may be such that this effect is smoothed out, although the "precipitous fall" Kattawar and Adams (1978) note in their "radiance vs height distribution" plot hints at this property (see their Fig. 7a).

In the optically deeper coma ($\tau_0 = 3$), long optical paths obscure the nucleus and smooth out the intensity discontinuities across the limb; the nucleus is outlined by a shallow trough in intensity rather than an abrupt jump. High scattering conditions lead to an apparent brighten-

FIG. 3. Symmetric coma, $\tau_0 = 0.5$, for varying phase angle. (a) $\theta_0 = 0°$: The Sun is directly behind the observer and we see backscattered light. "Isophotes" are circular about the nucleus, and limb brightening is evident. (b) $\theta_0 = 45°$: A bright crescent of light forms on the sunward side of the image. The abrupt jump in intensity across the limbs of the nucleus is enhanced in the multiply scattered component. (c) $\theta_0 = 135°$: The nucleus appears relatively darker than its surroundings because it blocks some sunlight. (d) $\theta_0 = 180°$: The nucleus eclipses the Sun.

FIG. 4. Symmetric coma, $\tau_0 = 3$, for varying phase angle. (a) $\theta_0 = 0°$: Obscured by dust, the nucleus is barely resolvable, and the center of the image has an intensity peak. (b) $\theta_0 = 45°$: Variation in the I_1 component in almost smooth across the limbs, but jumps in intensity develop in the $I_{\geq 2}$ component. (c) $\theta_0 = 135°$: A bright maximum forms distinctly to the left of a dark disk; the nucleus casts a shadow in the right-hand portion of the image. (d) $\theta_0 = 180°$: The nucleus eclipses the Sun. Scattered light fills in the antisunward shadow.

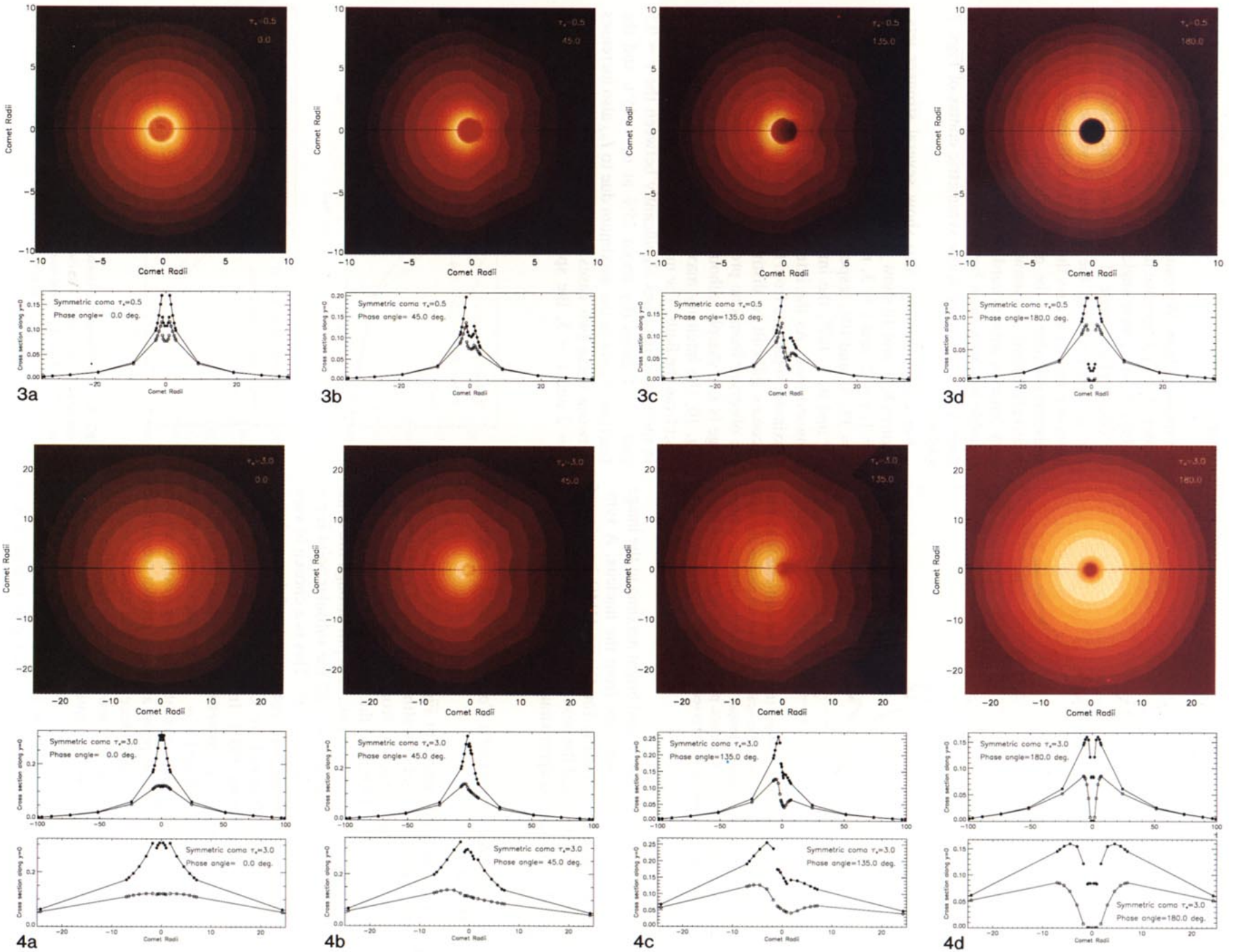
Comet Radii
Symmetric coma τ=0.5
Phase angle= 0.0 deg.
Symmetric coma τ=0.5
Phase angle= 45.0 deg.
Symmetric coma τ=0.5
Phase angle=135.0 deg.
Symmetric coma τ=0.5
Phase angle=180.0 deg.
Cross section along y=0
3a
3b
3c
3d
Symmetric coma τ=3.0
Phase angle= 0.0 deg.
Symmetric coma τ=3.0
Phase angle= 45.0 deg.
Symmetric coma τ=3.0
Phase angle=135.0 deg.
Symmetric coma τ=3.0
Phase angle=180.0 deg.
4a
4b
4c
4d

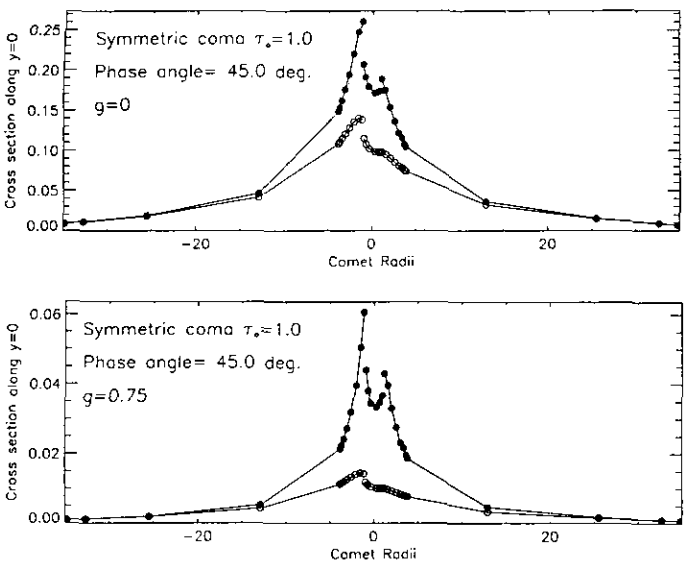

FIG. 5. Comparison of isotropic (top) and forward-peaked scattering (bottom) for $\theta_0 = 45°$. Isotropic scattering reverses photon direction efficiently and gives a brighter image. For forward-scattering, a larger fraction of light is due to $I_{\geq 2}$, since photons must be scattered many times for their direction to be reversed.

ing of the nucleus center, and bright maxima in the image which are distinctly separate from the nucleus. A symmetric coma is unrealistic for Giotto HMC imaging of Halley, however, and the next sequence of images shows a model designed to approximate the Giotto viewing conditions.

3b. Simulated Images of a Coma with an Axisymmetric Dust Jet

The simulated images in Fig. 7 show a coma with an axisymmetric dust jet of width $W = 0.3$ radian extending in the sunward direction from the subsolar point. Its strength is $X = 14.0$, and the background optical depth $\tau_0 = 0.05$. The transverse optical depth through the coma on a line-of-sight passing just off the subsolar point is $\tau \approx 0.5$ when viewed from $\theta_0 \approx 90°$. This is a chosen in view of Thomas and Keller's recent estimate of the maximum optical depth observed by Giotto HMC of about 0.4 (Thomas and Keller 1991). In this case, the coma was truncated at $r_{max} = 15$ comet radii for calculation of $I_{\geq 2}$. We again set $g = 0$ and $\lambda = 1$ to put an upper limit on scattering effects. The jets observed by Giotto are not exactly at the subsolar point and may project toward the camera. We cannot reproduce this effect exactly with an axisymmetric jet, but by viewing an axisymmetric jet at two phase angles, we can qualitatively investigate scattering effects present in the images.

For Fig. 7a, $\theta_0 = 45°$, the jet projects out toward the observer, and the specific intensity builds to a peak near the sunward limb. We cannot see the nucleus edge in the center of the jet because it is obscured by scattered light. In Fig. 7b, the phase angle is $\theta_0 = 107°$, corresponding to the Giotto phase angle at the time of the HMC imaging. The sunward edge of the nucleus is visible as a sharp jump in intensity across the limb. In both images the dark antisunward edge of the nucleus is silhouetted against a relatively bright antisunward coma. Since the coma is very tenuous antisunward of the nucleus, there is no detectable intensity peak beyond the antisunward limb (as there was in the spherically symmetric comas of Figs. 3 and 4).

For comparison we also show several stronger jets. Figures 8, 9, and 10 show jets of transverse optical depth $\tau \approx 1$, $\tau \approx 2$, and $\tau \approx 3$, respectively. The strengths are $X = 33$, 70, and 108, respectively. In Fig. 8, for both $\theta_0 = 45°$ and $\theta_0 = 107°$, the intensity builds to a peak at the sunward limb. As the intensity of the jet increases, this maximum separates from the limb and moves sunward, it becomes difficult to distinguish a jet projecting toward the observer from one projecting away, and the nucleus edge is not sharply silhouetted at $\theta_0 = 107°$. For $\tau = 3$, Fig. 10, the intensity maximum in the jet is clearly distinct from the limb. The magnitude of the peak brightness in the image increases significantly between the $\tau \approx 0.5$ and $\tau \approx 1$ cases (by about 25% at $\theta_0 = 45°$), and the fraction of light in the maximum due to $I_{\geq 2}$ also increases between these two cases. With increasing jet strength, $\tau \approx 2$ and $\tau \approx 3$, the spatial extent of the illuminated

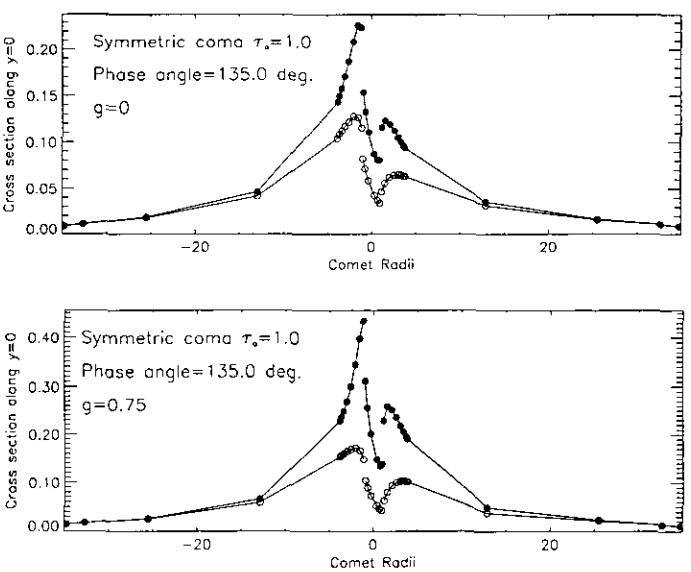

FIG. 6. Comparison of isotropic (top) and forward-peaked scattering (bottom) for $\theta_0 = 135°$. For isotropic scattering, the image is dimmed close to the limb. Forward-scattering allows light to penetrate efficiently through even the deepest portion of the coma, and brightness peaks at the limb.

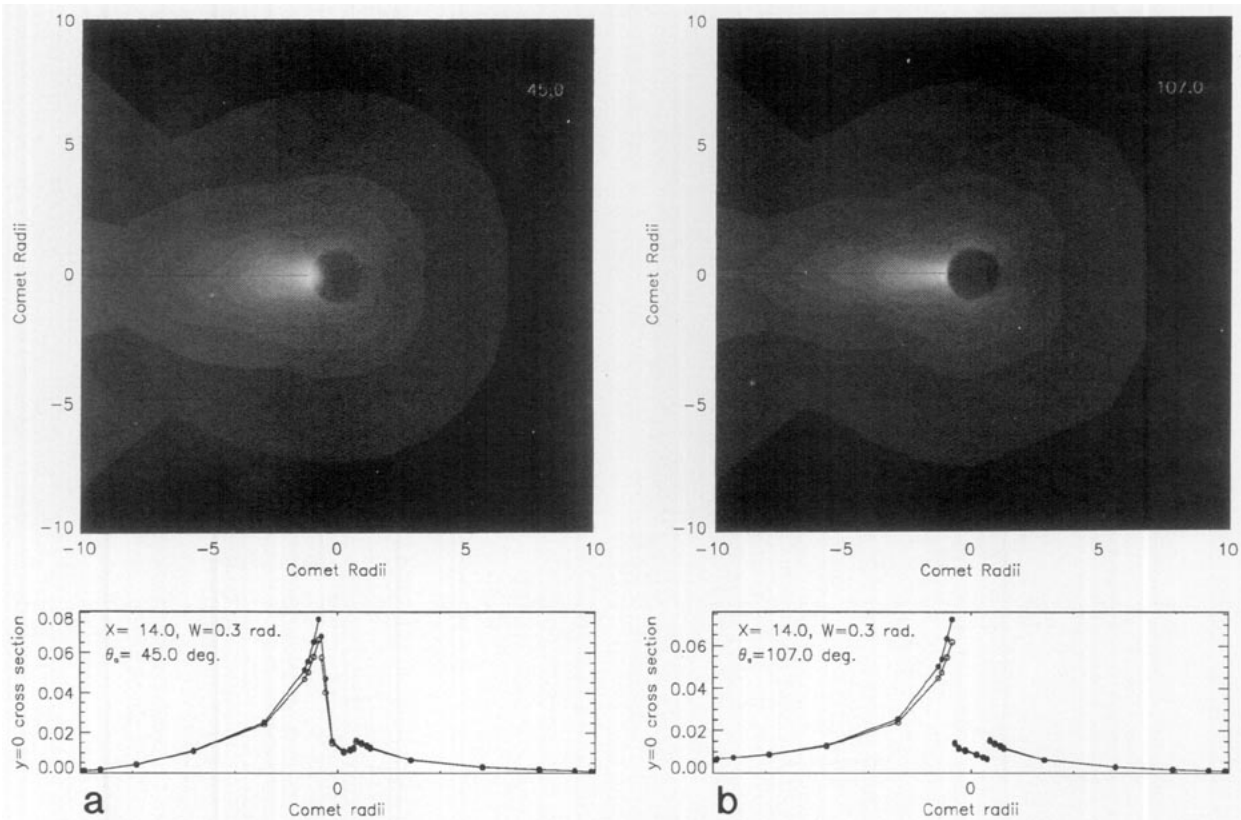

FIG. 7. Simulated images of a coma with an axisymmetric dust jet; transverse optical depth $\tau \approx 0.5$. (a) $\theta_0 = 45°$: The jet projects out toward the observer. The nucleus edge in the center of the jet is obscured by scattered light. (b) $\theta_0 = 107°$: The jet projects away from the observer, and the sunward edge of the nucleus is visible as a sharp jump in intensity across the limb.

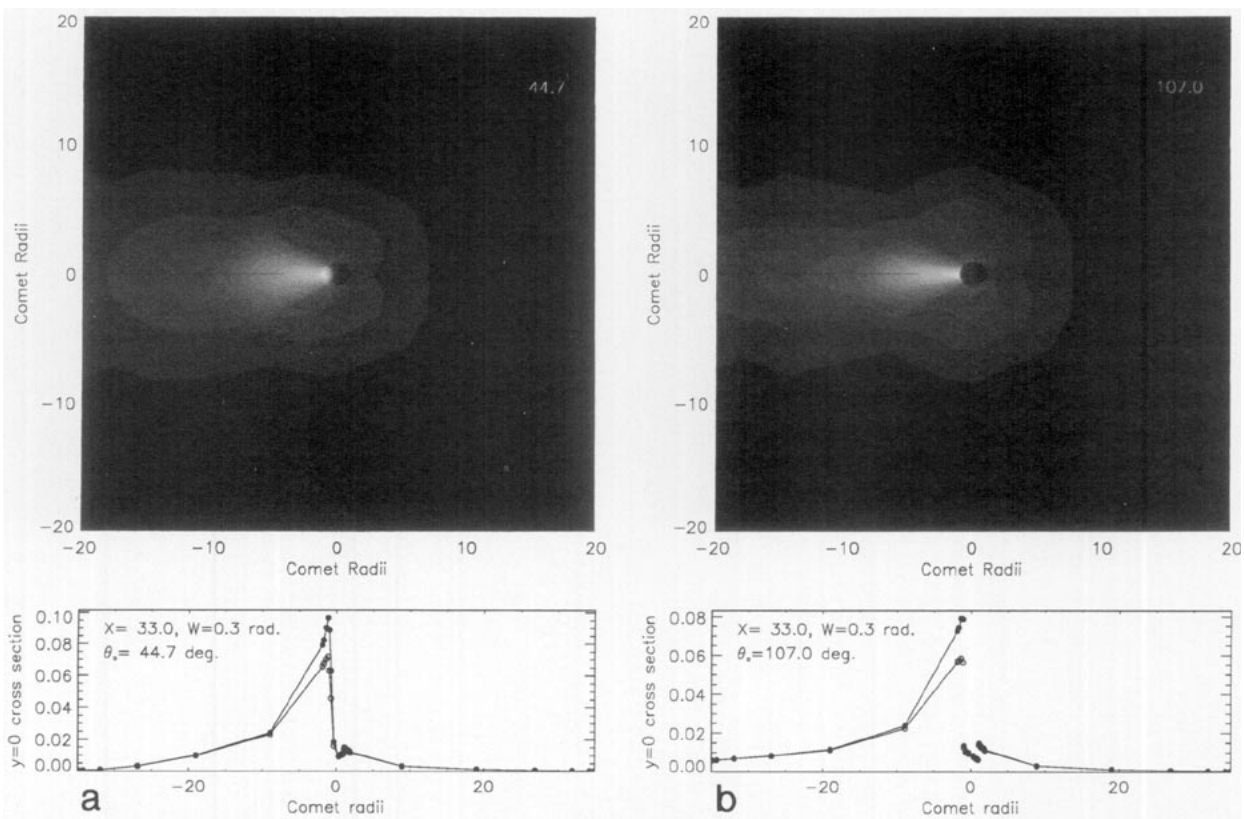

FIG. 8. Simulated images of a coma with an axisymmetric dust jet; transverse optical depth $\tau \approx 1$. (a) $\theta_0 = 45°$: The magnitude of the brightness peak in the center of the jet increases by about 25% over the $\tau \approx 0.5$ case. (b) $\theta_0 = 107°$: As in Fig. 7b, brightness peaks at the limb, sharply delineating the nucleus edge.

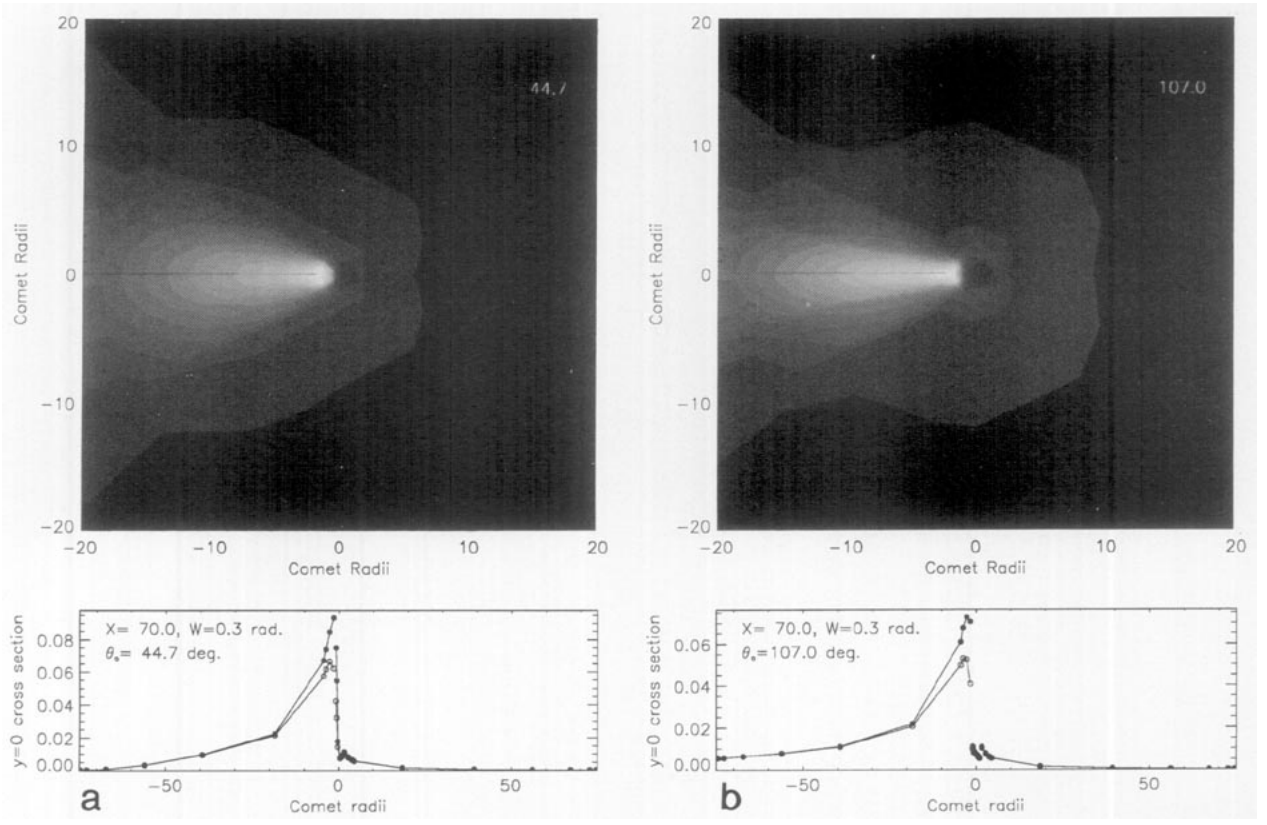

FIG. 9. Simulated images of a coma with an axisymmetric dust jet; transverse optical depth $\tau \approx 2$. (a) $\theta_0 = 45°$: The magnitude of the brightness peak in the center of the jet decreases slightly from the $\tau \approx 1$ case. (b) $\theta_0 = 107°$: The brightness peak separates from the limb and moves sunward.

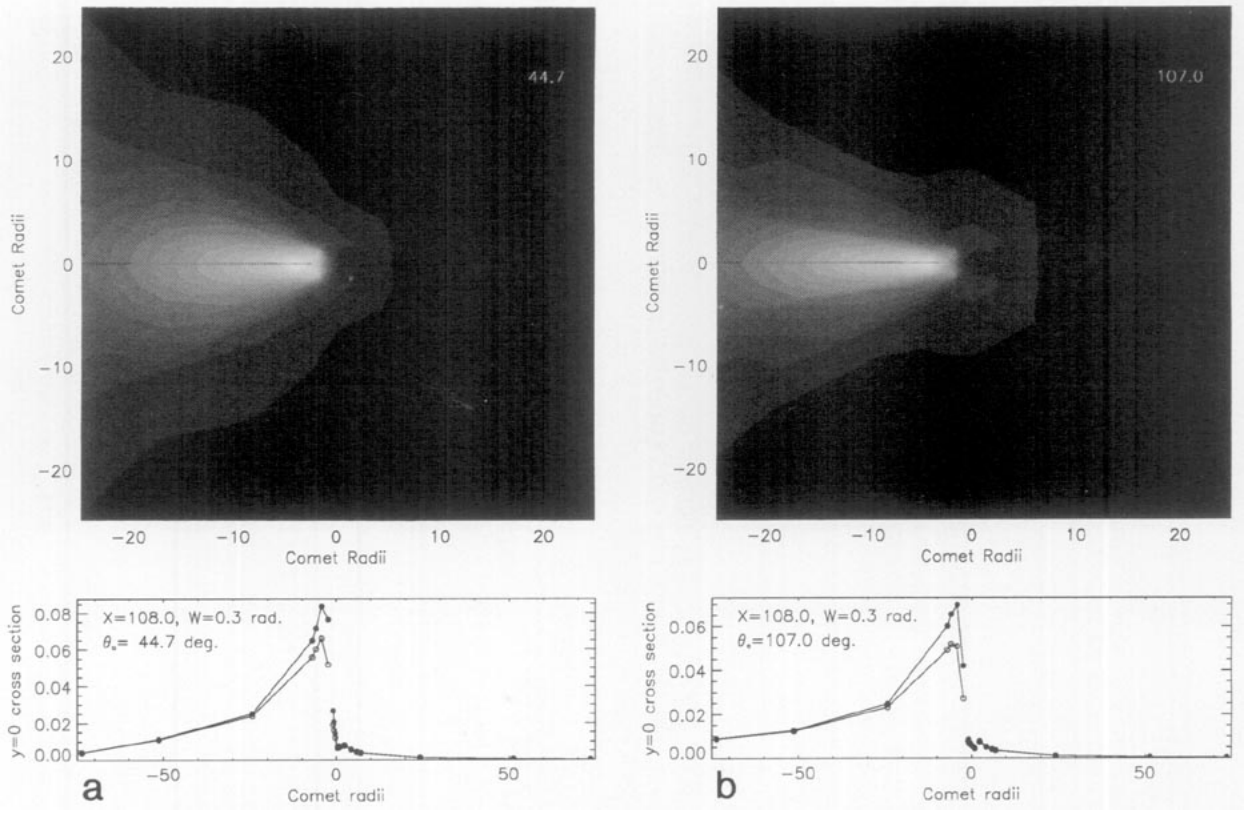

FIG. 10. Simulated images of a coma with an axisymmetric dust jet; transverse optical depth $\tau \approx 3$. (a) $\theta_0 = 45°$: The magnitude of the brightness peak in the center of the jet continues its gradual decrease from the $\tau \approx 1$ case. (b) $\theta_0 = 107°$: The brightness peak is now far to the left of the limb, and it is difficult to distinguish a jet projecting toward the observer from a jet projecting away. The nucleus edge is no longer sharp.

portion of the image increases, but the peak brightness actually decreases slightly from the $\tau \approx 1$ case.

The overall appearance of the jets resembles those observed by the Giotto HMC. In all cases multiple scattering is significant only near the base of the jet on the sunward limb of the nucleus. With the high-scattering $\lambda = 1$, light scattered two-or-more times accounts for about 10–15% of the signal for $X = 14$ ($\tau \approx 0.5$), and about 30% for $X = 108$ ($\tau \approx 3$). Multiple scattering does not accentuate bright/dark features as it does in the optically deeper symmetric comas of Figs. 3 and 4. Thomas and Keller are justified in neglecting multiple scattering in their image analysis, especially since λ may be considerably less than 1. In view of our results the jets observed by Giotto appear rather dim if their transverse optical depth is on the order of 1/2: the strongest part of the jet was only 50% brighter than the surrounding nucleus (Keller *et al.* 1987), which supports the idea of dark, low-scattering material. The jets observed by Giotto appear more concentrated and collimated, indicating the model jet we have used might be replaced with a cone of emission at the nucleus surface; we address this in the next section.

3c. Simulated Images of a Hollow Cone of Emission Centered at the Subsolar Point

Both Kitamura (1986) and Körösmezy and Gombosi (1990) found time-dependent hydrodynamic flow properties which tend to "hollow out" an axisymmetric dust jet. To model this phenomenon, we modified the extinction profile in Eq. (2) by replacing θ with $\theta - \theta_c$. This makes a conical shell of dust about the subsolar point, with opening angle θ_c. We set $\theta_c = 0.5$ rad $= 28°$, $W = 0.1$ rad, $X = 10$, and $\tau_0 = 0.05$. The grey-scale images in Fig. 11 demonstrate that the appearance of the coma is very sensitive to viewing geometry. In Fig. 11a, $\theta_0 = 25°$, the observer is just "inside" the cone. We see a bright cone edge to the right of the dark subsolar point. In Fig. 11b, $\theta_0 = 45°$, and we are now "outside" the cone; the base of the cone gives a bright "double-flare" structure. In Fig. 11c, $\theta_0 = 90°$, the conical structure is most evident. In Fig. 11d, $\theta_0 = 135°$, the cone structure is lost, and we see a uniform band of light on the left limb.

The results for $\theta_0 = 90°$ appear strikingly similar to the HMC image of Halley's "northern area of activity," shown (for example) in photographs in an article by Thomas and Keller (1987). In that article Thomas and Keller consider the possibility that the "northern area" was the hollow cone predicted by hydrodynamic simulations, but argue against its presence in the images. There were filaments of dust which emanated from at least four small sources near the base of the "northern area." Thomas and Keller suggest that these filaments merge into the outflow and appear as streaks which give the impression of a single hollow cone; but they acknowledge their argument is not conclusive.

4. SIMULATIONS OF AZIMUTH-INTEGRATED INTENSITY

The jets observed by Giotto HMC appear as overlapping cones of emission, and Huebner *et al.* (1988) showed that viewing geometry of the complicated surface emission can account for the observed deviation from ρ^{-1} slope in intensity. Thomas and Keller (1990) considered the integral of the observed intensity over viewing azimuth Φ'' for a given line-of-sight impact parameter ρ, multiplied by the impact parameter: in our notation,

$$Z = \rho \int_0^{2\pi} (I_1 + I_{\geq 2})\, d\Phi''. \tag{6}$$

Thomas and Keller called $Z/(2\pi)$ the "azimuthal average intensity." They derived an approximate relation between Z and the surface integral of dust flux over a Gaussian volume enclosing the nucleus: again in our notation,

$$\oint n\mathbf{v} \cdot d\mathbf{S} \propto \langle \nu \cos \chi \rangle\, Z \tag{7}$$

where ν is the speed of the dust, and χ the angle between the dust velocity and the surface normal of a "view cone" (see Appendix B). By examining the quantity Z for Giotto HMC images, and making heuristic arguments about the spatial behaviour of $\langle \nu \cos \chi \rangle$, Thomas and Keller used Eq. (7) to put constraints on the viewing geometry effects discussed by Huebner *et al.*, and suggest that the depletion of intensity near the nucleus cannot be accounted for exclusively by such effects.

In Appendix B we summarize the argument made by Thomas and Keller, and clarify some points. Impact parameter ρ characterizes the size of a volume enclosing the nucleus in Eq. (7), and by Gauss' Law, if dust particles are not born in the outflow (i.e., by fragmentation), the product $\langle \nu \cos \chi \rangle\, Z$ should be constant with ρ. Observations from Giotto HMC data indicate the quantity Z is constant beyond about 100 km of the nucleus, but depleted near the nucleus (see Thomas and Keller 1990, Fig. 6). Regardless of the angle-dependence of the surface source, if dust particles follow constant-velocity radial trajectories, the term $\langle \nu \cos \chi \rangle$ will be nearly constant; this should be its background and asymptotic behavior. Thomas and Keller examine possible dust acceleration mechanisms and argue that net acceleration effects should either not significantly increase $\langle \nu \cos \chi \rangle$ near the nucleus or decrease it. They argue, therefore, that the extent to which Z is depleted near the nucleus indicates particle fragmentation is occurring in the outflow.

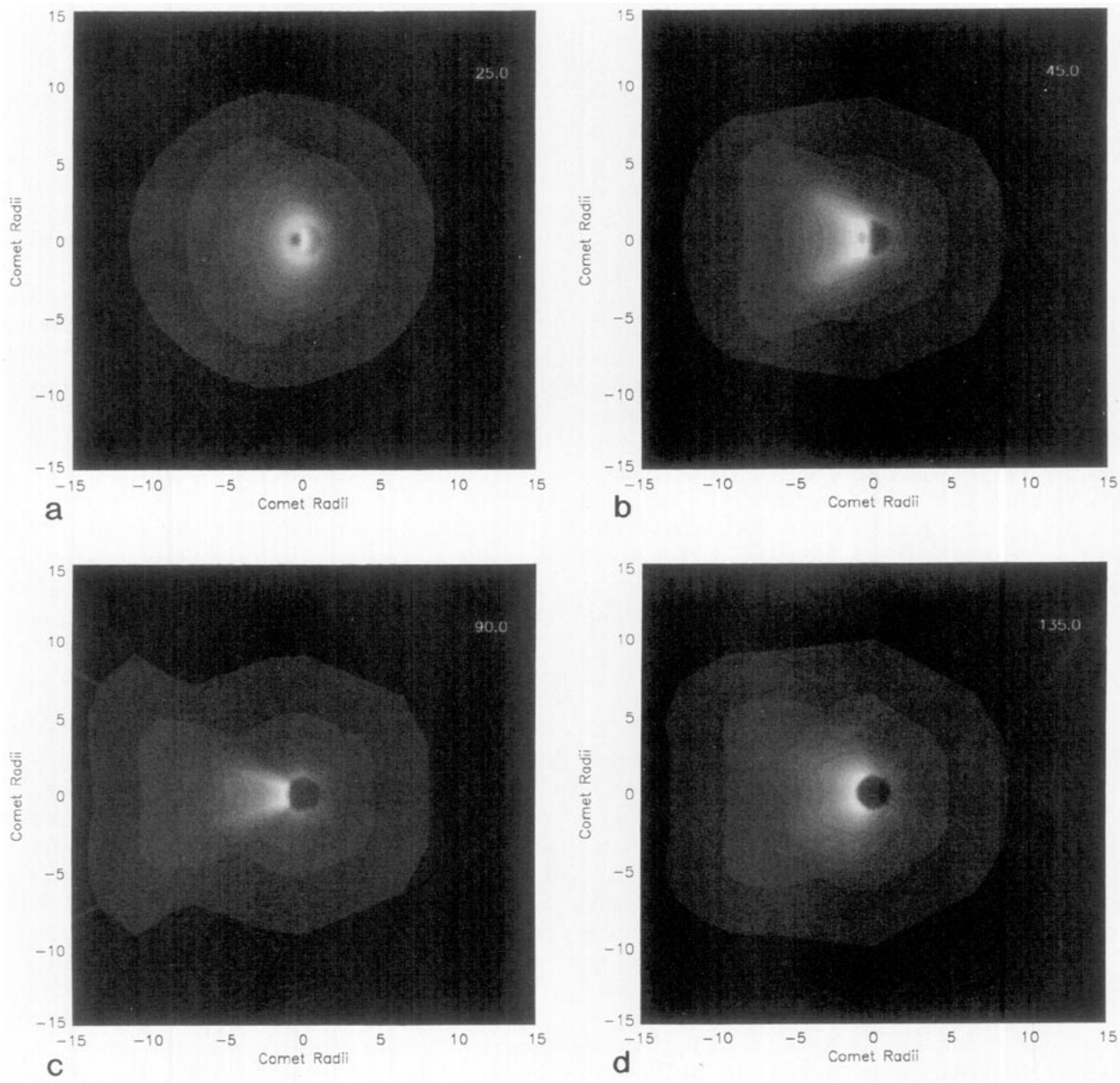

FIG. 11. Simulated images of a coma with a conical shell of dust about the Sun–comet axis. (a) $\theta_0 = 25°$: The opening angle of the dust cone is 28°, so the observer is "inside" the cone. The dark nucleus is visible in the center. (b) $\theta_0 = 45°$: The observer is "outside" the cone of dust. (c) $\theta_0 = 90°$: The cone is viewed from the side, and resembles the "northern area of activity" observed at Halley by the Giotto HMC. (d) $\theta_0 = 135°$: The cone appears as a bright band, and its structure is not visible.

Most of Thomas and Keller's analysis assumes optically tenuous conditions, where line-of-sight attenuation and multiple scattering can be neglected. We investigate the extent to which deviations from the unattenuated single scattering approximation, Eq. (B2) in Appendix B, will affect the measure of Gauss' Law. Line-of-sight attenuation will deplete the azimuth-integrated intensity, and multiple scattering will enhance it, acting as an effective source in the Gaussian volume analysis. To give a precise quantification of these effects, we calculated Z for our model comas.

Figure 12a shows Z for the spherically symmetric coma of $\tau_0 = 1$, $g = 0$, $\lambda = 1$, observed at $\theta_0 = 90°$. Again, this case accentuates all transport effects. The single-scattered light, shown in open circles at each direction angle ordinate, shows the effect of strong line-of-sight attenuation near the nucleus. At this high optical depth, the overall depletion in the single-scattered light for the points

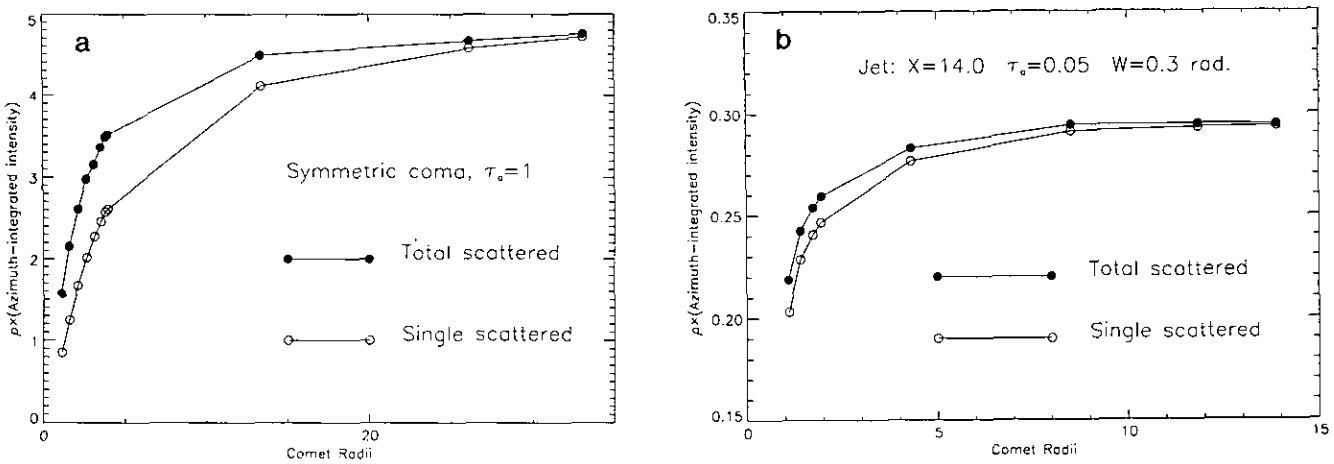

FIG. 12. The quantity $Z = \rho \times$ (azimuth-integrated intensity), plotted versus ρ.

nearest the nucleus limb in the image reaches about 75%. The total scattered light, $I_1 + I_{\geq 2}$, is enhanced over the single scattered light near the nucleus. Far from the nucleus the $I_{\geq 2}$ component becomes dim and the single scattered light accounts for an increasing fraction of the signal. With decreasing line-of-sight attenuation the quantity tends asymptotically to the constant value implied by Eq. (B3).

Figure 12b shows Z for the more realistic axisymmetric dust jet case, for the conditions described in Fig. 7. With a transverse optical depth of 0.5, there is less dust present around the nucleus than in the spherically symmetric coma of Fig. 12a, and both line-of-sight attenuation and multiple scattering are greatly reduced over the spherically symmetric case. Both effects are apparent only very near the nucleus. For the points nearest the nucleus limb in the image plane, the overall depletion in I_1 is almost 30%. Recalling Eqs. (2)–(4), the jet model is equivalent to constant-speed radial outflow from a point source (with angular source variation), and as discussed in Appendix B, $\langle \cos \chi \rangle$ is virtually constant for these conditions. With increasing ρ, line-of-sight attenuation diminishes, and the $I_{\geq 2}$ component becomes negligible. The quantity Z is then well-approximated with unattenuated single-scattered light, and is proportional to $\rho \int d\Phi'' \int nds$, which is constant, due to its relation to a Gaussian integral enclosing a constant source, as described by Eq. (B8) in Appendix B.

There is no question optical depth attenuation can account for the general shape of the observed profiles (compare Thomas and Keller 1991, Fig. 4). We show that for an idealized jet with transverse optical depth of 1/2, a 30% depletion can be accounted for; whereas the observed depletion is only about 20%. However, Thomas and Keller (1991) argue that Giotto in situ measurements combined with HMC images prove optical depths are insufficient to account for the observed depletion by a factor of 2.

Our results quantify multiple scattering as a source of light which decreases with ρ; multiple scattering therefore tends to steepen the slope of the azimuth-integrated intensity rather than flatten it. Our results also give an exact calculation of the attenuation of the single-scattered light, which does tend to flatten the slope. The significance of multiple scattering and attenuation depends on the optical depth of the coma. The multiple scattering effects will also depend strongly on the scattering properties of the dust grains.

5. DISCUSSION

Our results give a survey of light scattering effects present in near-nucleus inner coma imaging. Multiple scattering will brighten jet features and may silhouette the antisunward limb. Exaggerated limb brightening effects occur for optically deep comas. The optical depth for the model jet in Fig. 7 is small enough that no dramatic effects are present, which reinforces Thomas and Keller's analysis. The maximum optical depths observed by Giotto HMC are well constrained as being less than 1 (Keller *et al.* 1987); Thomas and Keller (1991) estimate an optical depth of 0.4 transverse through the base of the brightest jet, but they point out that if the fly-by had occurred a day later the nucleus might not have been visible due to an outburst. So although the dramatic effects we show for symmetric comas of $\tau_0 = 0.5$ and 3 are probably not present in Giotto HMC images, our approach should be useful for future comet observations.

Multiple scattering effects will depend on the optical properties, P, and especially λ, of the coma material. Divine *et al.* (1986) reviewed optical properties of comet dust. Phase functions for comet dust are thought to be

forward peaked (perhaps $0.5 \leq g \leq 0.8$; see Divine *et al.*, Fig. 20). They reported estimates of the single scatter albedo which were uncertain, but quite absorptive, ranging from $\lambda = 0.05$ to 0.3–0.5. More recent work (Dollfus 1989, Mukai *et al.* 1987, 1991) suggests that scattered light is determined by two separate types of particles: large dark aggregate flakes, and tiny high-scattering grains. Dollfus reviewed the polarization effects observed in Halley's coma; observations show a distinct signature of fluffy, very dark aggregates of small particles, with the aggregated flake much larger than the wavelength of scattered visible radiation, and the small particles of which it is composed less than 10 μm in size. Within 100 km of Halley's nucleus, Dollfus reports the coma was much more reflective, and the slope of polarization with phase angle is altered; he explains this by either a dense cloud of small grains or ice crystals. Mukai *et al.* (1987) used polarization data to fit a refractive index for coma dust of about $(n, k) = (1.385, 0.035)$, which is not necessarily absorptive, and may suggest an additional presence of smaller grains with a higher-scattering nature. Tiny grains may also dominate polarization during outburst conditions, at large phase angles (80–110°: Dollfus 1989, Mukai *et al.* 1991), and in jets (Eaton *et al.* 1988, 1991). In support of a two-component dust coma, Hanner and Campins (1986) interpret observed thermal emission from comet Bowell as coming from large dirty ice grains of low albedo and a component of scattered light as coming from small cold ice grains of higher albedo.

Questions remain concerning the appearance of the jets in Giotto HMC images, modeling of particle evolution in the outflow, and related dust–gas flow in the coma, such as near-surface tangential breezes and jet structure. The Huebner *et al.* analysis of viewing geometry effects essentially assumes collisionless outflow: the jets overlap but do not interact with each other. Kitamura (1990) has modeled the three-dimensional hydrodynamic interaction between coma jets with dust particle-size as a parameter. The resulting jet structure depends on the density of the background coma; in general the colliding jets each have a hollow-cone structure. The cones are separated by two shock fronts, with a sheet of compressed gas between the fronts which may extend to 100 km from the nucleus. Small dust particles concentrate in the compressed gas sheet and should leave a signature in scattered polarized light.

Thomas and Keller's use of a Gaussian volume to demonstrate the occurrence of particle fragmentation circumvents viewing geometry problems, but quantification of variation of the term $\langle \nu \cos \chi \rangle$ in function of ρ is very difficult (see Appendix B). Kitamura's work emphasizes that the complicated acceleration of outflowing dust should be modeled with a realistic hydrodynamic calculation and a spectrum of particle sizes. A recent one-dimensional hydrodynamic model with dust fragmentation by Konno *et al.* (1992) indicates an extremely high fragmentation rate would be required to account for the observed deviations from a ρ^{-1} dependence in the intensity profiles; they conclude other processes must be at play.

Jet outflow from the nucleus surface will perturb a comet's orbit. The jets observed at Halley appeared collimated; this collimation may enhance the efficiency of momentum transfer to the nucleus (Sekanina 1990). It is not clear if jet collimation is an effect of surface emission or if it occurs in the outflow. Körösmezey and Gombosi (1990) discovered a collimated spike which can form in a jet due to dust–gas hydrodynamic effects. Jet activity should lead to strong erosion of the nucleus at the vent (Sekanina 1990), and emission from a deep vent might also explain the collimation.

Three-dimensional dust–gas hydrodynamic models of inner comas which include a particle-size cascade due to fragmentation, and comet nucleus models, will provide input for answering these questions. The images taken by both the Giotto HMC and by Weaver *et al.* (1992) with the HST indicate the axisymmetric jet model should be a fundamental tool for future image analysis. The spherically symmetric model may be valid for new comets or young comets either before a nonvolatile mantle develops or following a purge ("blow-off") of their mantle (see for example the Rickman *et al.* 1991 model of short-period comet aging). As demonstrated in the hollow cone case of Fig. 11, the appearance of flow patterns can be very sensitive to viewing geometry, and our code will provide an essential link between dust–gas hydrodynamic modeling of comas and observations.

6. CONCLUSION

We have applied the numerical solution of Paper I to the simulation of images of a coma as it would appear to a near-flying satellite such as Giotto. The appearance of symmetric comas and dust jets was examined in detail, nucleus visibility was studied, we considered the effect of forward-scattering, and single- and multiple-scattering effects were quantified. We examined simulated images of a coma with hollow cone of dust, as predicted by dust–gas hydrodynamic modeling. The cone's appearance was very similar to the "northern area of activity" on Halley, observed by the Giotto HMC.

Keller *et al.* (1987) and Thomas and Keller (1990) neglected multiple scattering in analyzing Giotto HMC images, and our results confirm this approximation. The magnitude of the scattering effects we have noted depends on the optical depths and on the optical properties of the scattering material in the coma. The optical depths observed by Giotto at Halley were relatively thin, but

during an outburst they should be much greater. The results presented here indicate that in such an outburst, multiple scattering might play a significant role within about 10 comet radii from the nucleus. Estimates of a single scatter albedo λ for comet dust are quite low, but strong evidence exists for at least some high-scattering material in the coma.

We also quantified line-of-sight attenuation and multiple scattering effects in the azimuth-integrated intensity used by Thomas and Keller (1990) to estimate dust particle fragmentation. We showed that line-of-sight attenuation can easily account for general shape of the intensity profiles observed by Giotto at Halley, but we must defer to their arguments based on in situ measurements of Halley's dust environment.

The image simulation code we have developed will be an essential link between future dust–gas hydrodynamic modeling of comas and observations. Working in axisymmetric geometry allows great flexibility, and our approach should be useful for work related to Giotto HMC images, interpretation of new imaging (such as the HST) which might resolve comet nuclei, and any future comet fly-by missions.

APPENDIX A: CONSTRUCTING AN IMAGE FROM THE NUMERICAL SOLUTION

To simulate an image, we must interpolate the specific intensity emerging along discrete ordinates at the outer edge of the coma, $r = r_{max}$. Referring to Fig. 2, the observation position is $\mathbf{r}_0(r_0, \theta_0, 0)$. The discrete ordinates are specified in the spherical reference at each position in the coma; we denote this reference with a prime, so that a given direction ordinate is $\boldsymbol{\Omega}(\Theta_i', \Phi_j')$. A few sample ordinates are shown emerging from the top of the coma. For ease in drawing, we suppress the third dimension by considering the special case where $\Phi'' = 0$ and $\Phi' = 0$; as a concrete example, the direction angle is chosen as $\Theta' = \Theta_i'$. Coordinates in the reference rotated to the observation point are denoted with a double prime.

For each $\Theta_i' < \pi/2$, and every Φ'' ($0 \le \Phi'' \le 2\pi$), there is a position $\mathbf{r}(r_{max}, \theta, \phi)$ and direction $\boldsymbol{\Omega}(\Theta_i, \Phi) = \mathbf{R}_z(-\phi) \cdot \mathbf{R}_y(-\theta) \cdot \boldsymbol{\Omega}(\Theta_i', \Phi')$ such that $\mathbf{r} + s\boldsymbol{\Omega} = \mathbf{r}_0$ for some s. That is, a light ray originating at $\mathbf{r}$ in the direction $\boldsymbol{\Omega}$ intercepts $\mathbf{r}_0$ and contributes to the image. In order to interpolate the intensity of this ray from our numerical solution, we must determine θ and Φ'.

For a given Θ_i' and Φ'' we proceed to find θ and Φ'. We first solve the system

$$\begin{aligned} \cos(\Theta'') &= \cos(\theta'' - \Theta_i') \\ r_0 &= r_{max} \cos\theta'' + s \cos\Theta_i' \\ s &= r_0 \cos\Theta'' - r_{max} \cos\Theta_i' \end{aligned} \tag{A1}$$

for s, $\cos\Theta''$, and $\cos\theta''$. Then the relation

$$\mathbf{r}(r_{max}, \theta, \phi) = \mathbf{R}_y(-\theta_0) \cdot \mathbf{r}(r_{max}, \theta'', \Phi'' - \pi) \tag{A2}$$

determines the position angles θ and ϕ on the outer edge of the coma where the observed light originates. For a given Φ'', the appropriate value of Φ' is determined from the relation

$$\mathbf{R}_y(\theta) \cdot \mathbf{R}_z(\phi) \cdot \mathbf{r}_0(r_0, \theta_0, 0) = \mathbf{r}(r_{max}, 0, 0) + s\boldsymbol{\Omega}(\Theta_i', \Phi'). \tag{A3}$$

To generate an entire image, for each $\Theta_i' < \pi/2$ we scan through the image plane azimuth Φ'' at convenient values (such that $0 < \Phi'' < \pi$, due to symmetry). For each Φ'', we determine the position angle of emission θ, and the direction azimuth Φ'. A single point in a simulated image is thus $I(r_{max}, \theta, \Theta_i', \Phi')$, it is found by interpolating the numerical solution on the angle grid, θ, and interpolating in direction azimuth, Φ'. The point's location in the image plane is $x'' = \sin\theta'' \cos(\Phi'' - \pi)$, $y'' = \sin\theta'' \sin(\Phi'' - \pi)$, and the impact parameter, ρ, is approximately equal to $(x''^2 + y''^2)^{1/2}$.

APPENDIX B: EXAMINATION OF THOMAS AND KELLER'S ARGUMENT FOR DUST FRAGMENTATION

As a reference for future dust–gas flow modelling, we summarize and clarify Thomas and Keller's argument.

(a) *Idealized Intensity Profiles for Tenuous Conditions*

Under optically tenuous conditions, single-scattered light should be a good approximation for the scattered radiation field. The single-scattered component at the observation point $\mathbf{r}_0$ and in direction $\boldsymbol{\Omega}$ is

$$I(\mathbf{r}_0, \boldsymbol{\Omega}) \cong I_1(\mathbf{r}_0, \boldsymbol{\Omega}) = \frac{S}{4} \int_0^\infty ds\, e^{-\int_0^s ds'\alpha(\mathbf{r}_0 - s'\boldsymbol{\Omega})}\, e^{-\int_0^\infty ds'\alpha(\mathbf{r}_0 - s\boldsymbol{\Omega} - s'\boldsymbol{\Omega}_0)} \lambda P(\boldsymbol{\Omega} \cdot \boldsymbol{\Omega}_0)\alpha(\mathbf{r}_0 - s\boldsymbol{\Omega}). \tag{B1}$$

If we neglect all attenuation, assume the optical properties λ, P, and σ are spatially constant, and substitute $\alpha = n\sigma$, we have

$$I_1(\mathbf{r}_0, \boldsymbol{\Omega}) \cong \frac{S\lambda}{4} \sigma P(\boldsymbol{\Omega} \cdot \boldsymbol{\Omega}_0) \int_0^\infty ds\, n(\mathbf{r}_0 - s\boldsymbol{\Omega}). \tag{B2}$$

For a spherically symmetric coma, corresponding to constant radial outflow from an isotropic source, and $r_0 \gg \rho$, the integral in Eq. (B2) can be approximated as (see also Eq. A2 of Paper I),

$$I_1(\mathbf{r}_0, \boldsymbol{\Omega}) \cong 2\left(\frac{S\lambda}{4}\right) \sigma P(\boldsymbol{\Omega} \cdot \boldsymbol{\Omega}_0) \int_0^{\sqrt{r_0^2 - \rho^2}} ds\, n(\mathbf{r}_0 - s\boldsymbol{\Omega}) = \frac{S\lambda}{4} P(\boldsymbol{\Omega} \cdot \boldsymbol{\Omega}_0) \left(\frac{\pi R \tau_0}{\rho}\right). \tag{B3}$$

Therefore we expect that for constant radial outflow from an isotropic source, the observed specific intensity will vary with impact parameter as ρ^{-1}. Giotto HMC line-of-sight intensities show a slope flatter than -1 near the nucleus, with the intensity effectively "depleted" by about 20% (see Figs. 6d and 6e in the Thomas and Keller 1990 article).

As long as the radial dust distribution varies approximately (or at least asymptotically) as r^{-2}, the integrand will be sharply peaked near the tangent point, $s = (r_0^2 - \rho^2)^{1/2}$. If we limit the range of integration to a small region about the tangent point, $[(r_0^2 - \rho^2)^{1/2} - \delta, (r_0^2 - \rho^2)^{1/2} + \delta]$, where $\rho \ll \delta \ll r_0$, Eq. (B2) becomes

$$I_1(\mathbf{r}_0, \boldsymbol{\Omega}) \cong \frac{S\lambda}{4} \sigma P(\boldsymbol{\Omega} \cdot \boldsymbol{\Omega}_0) \int_{\sqrt{r_0^2 - \rho^2} - \delta}^{\sqrt{r_0^2 - \rho^2} + \delta} ds\, n(\mathbf{r}_0 - s\boldsymbol{\Omega}). \tag{B2'}$$

This property makes it possible to approximate the "view cone" as a cylinder (see further).

(b) *Relation to Gauss' Law*

We examine Thomas and Keller's analysis in detail. The volume enclosed by the lines-of-sight is actually an open-ended cone, but for a

very elongated cone the contribution from the open end is negligible, so only the surface integral over the side of the cone is considered:

$$\oint = \oint_{\text{side}} + \oint_{\text{end}} \cong \oint_{\text{side}}. \tag{B4}$$

The surface integral over the side of the cone is

$$\oint_{\text{side}} n\mathbf{v} \cdot d\mathbf{S} \equiv \int_0^{2\pi} d\Phi'' \int_0^L ds\, n(\mathbf{r}_0 - s\boldsymbol{\Omega})\, \mathbf{v}(\mathbf{r}_0 - s\boldsymbol{\Omega}) \cdot \left[\frac{\partial \mathbf{f}}{\partial \Phi''} \times \frac{\partial \mathbf{f}}{\partial s}\right]$$
$$= \int_0^{2\pi} d\Phi'' \int_0^L ds\, n(\mathbf{r}_0 - s\boldsymbol{\Omega}) |\mathbf{v}(\mathbf{r}_0 - s\boldsymbol{\Omega})|\, |\mathbf{f}_{\Phi''} \times \mathbf{f}_s| \cos\chi, \tag{B5}$$

where $\mathbf{f}$ is a mapping from the $(\Phi'' \times s)$ plane to the cone surface, given explicitly as $\mathbf{f} = [(s\rho/r_0)\cos\Phi'', (s\rho/r_0)\sin\Phi'', (s/r_0)(r_0^2 - \rho^2)^{1/2}]$, and where L is the length of the cone. The cosine of the angle between the velocity $\mathbf{v}$, and the surface normal, $\mathbf{f}_{\Phi''} \times \mathbf{f}_s$, is $\cos\chi$. The magnitude of the surface normal is

$$|\mathbf{f}_{\Phi''} \times \mathbf{f}_s| = \frac{s\rho}{r_0} \tag{B6}$$

so the cone size is characterized by ρ.

Again we assume the integrand will be sharply peaked near the tangent point, and restrict the range of integration to the small region about the tangent point. To motivate this, we note that for constant-velocity radial flow the cosine of the angle between the velocity and the surface normal is

$$\cos\chi = \frac{\rho}{|\mathbf{r}_0 - s\boldsymbol{\Omega}|} = \frac{\rho}{(s^2 + r_0^2 - 2s\sqrt{r_0^2 - \rho^2})^{1/2}}. \tag{B7}$$

Noting $Q = \nu n(R)$, we can introduce Eqs. (4), (B6), and (B7) into Eq. (B5) and evaluate the expression analytically; we can also write a similar equation for the end of the cone which can be evaluated analytically. It can be verified that the sum these two results is $4\pi R^2 Q$, which is the enclosed source. More importantly, we note that if we consider only the contribution from the cone side, Eq. (B5), and limit the interval of integration for the variable s to the small region near the tangent point, evaluating Eq. (B5) gives $2\pi R^2 Q(2 - (\rho/\delta)^2 + \ldots)$, which is the enclosed source accurate to order $(\rho/\delta)^2$. For concreteness, in Giotto image 3416, ρ = 10–40 km, $r_0 = 2.56 \times 10^4$ km; and for image 3056, ρ = 10–300 km, $r_0 = 1.24 \times 10^5$ km (see Thomas and Keller 1990, Table I and Fig. 6).

In the region of integration near the tangent point, $s \approx r_0$. We set $(s/r_0)\rho = \rho$ where it appears in the magnitude of the surface normal. It is necessary to make this approximation in order to introduce the observed intensity as an approximation to the surface flux integral. We arrive at

$$\oint_{\text{side}} n\mathbf{v} \cdot d\mathbf{S} \cong \langle \nu \cos\chi \rangle\, \rho \int_0^{2\pi} d\Phi'' \int_{\sqrt{r_0^2 - \rho^2} - \delta}^{\sqrt{r_0^2 - \rho^2} + \delta} ds\, n(\mathbf{r}_0 - s\boldsymbol{\Omega}), \tag{B8}$$

where $\langle \nu \cos\chi \rangle$ is an average value of $|\mathbf{v}| \cos\chi$. Making the approximation $I \approx I_1$, and substituting from Eq. (B2'), the right hand side becomes

$$\cong \frac{4\langle \nu \cos\chi \rangle \rho}{S\lambda\sigma} \int_0^{2\pi} \frac{I}{P(-\cos\theta_0)}\, d\Phi'' \tag{B9}$$

To a good approximation the scattering angle is constant, so the phase function can be taken outside the integral in Eq. (B9). Combining this with the relation (B4), we have

$$\oint n\mathbf{v} \cdot d\mathbf{S} \cong \frac{4\langle \nu \cos\chi \rangle Z}{S\lambda\sigma P(-\cos\theta_0)},$$

where

$$Z = \rho \int_0^{2\pi} I\, d\Phi''. \tag{B10}$$

Eq. (B10) provides a convenient way of eliminating effects due to complicated dust emission at the surface. If the right-hand side increases with ρ, the surface integral of the flux will increase with ρ, and by Gauss' Law the enclosed source must increase with ρ.

Evaluation of $\langle \nu \cos\chi \rangle$ is possible for the case of constant velocity radial outflow. In general

$$\langle \nu \cos\chi \rangle = \frac{\int_0^{2\pi} d\Phi'' \int_0^{\infty} (s\rho/r_0)\, \nu n \cos\chi\, ds}{\int_0^{2\pi} d\Phi'' \int_0^{\infty} (s\rho/r_0)\, n\, ds}. \tag{B11}$$

First consider a constant surface source, Q, and set ν = constant. Again truncating the interval of integration, substituting from Eqs. (4) and (B7), we have

$$\langle \cos\chi \rangle = \frac{\rho \int_{\sqrt{r_0^2 - \rho^2} - \delta}^{\sqrt{r_0^2 - \rho^2} + \delta} s\, ds/(r_0^2 + s^2 - 2s\sqrt{r_0^2 - \rho^2})^{3/2}}{\int_{\sqrt{r_0^2 - \rho^2} - \delta}^{\sqrt{r_0^2 - \rho^2} + \delta} s\, ds/(r_0^2 + s^2 - 2s\sqrt{r_0^2 - \rho^2})}$$
$$= \frac{1}{\arctan(\delta/\rho)\sqrt{1 + (\rho/\delta)^2}}. \tag{B12}$$

Since $\delta \gg \rho$, Eq. (B12) yields $\langle \cos\chi \rangle \cong 2/\pi$. This result is equivalent to taking the ratio of Thomas and Keller's Eqs. (16) and (18).

For the case of constant-velocity radial flow with angular variation of the source over the surface of the comet, $Q = Q(\theta)$, the average cosine is

$$\langle \cos\chi \rangle = \frac{\rho \int_0^{2\pi} d\Phi'' \int_{\sqrt{r_0^2 - \rho^2} - \delta}^{\sqrt{r_0^2 - \rho^2} + \delta} \frac{Q(\theta)\, s\, ds}{(r_0^2 + s^2 - 2s\sqrt{r_0^2 - \rho^2})^{3/2}}}{\int_0^{2\pi} d\Phi'' \int_{\sqrt{r_0^2 - \rho^2} - \delta}^{\sqrt{r_0^2 - \rho^2} + \delta} \frac{Q(\theta)\, s\, ds}{r_0^2 + s^2 - 2s\sqrt{r_0^2 - \rho^2}}}. \tag{B13}$$

The angle specifying the position of emission in the density profile of Eq. (4) can be determined from

$$\cos\theta = \frac{(s/r_0)\rho \sin\theta_0 \cos\Phi'' + \cos\theta_0 [r_0 - (s/r_0)\sqrt{r_0^2 - \rho^2}]}{(r_0^2 + s^2 - 2s\sqrt{r_0^2 - \rho^2})^{1/2}}. \tag{B14}$$

Eq. (B13) is very weakly dependent on ρ. We evaluated Eq. (B13) numerically for the Gaussian profile $Q(\theta)$ given by Eq. (4), r_0 = 1000 comet radii, the jet parameters of Fig. 7, with $\delta = 10\rho$, and using library Gauss quadrature in s and trapezoidal rule integration in Φ''. As ρ increases from 1.5 to 20 comet radii, the value of $\langle \cos\chi \rangle$ increases by 2% for $\theta_0 = 15°$, and negligibly for $\theta_0 = 45°$ and 90°.

(c) *Evidence for Particle Fragmentation in the Coma*

Thomas and Keller (1990) examine the validity of Eq. (B10) in detail. They present reasons why the optical properties λ and P should not vary significantly; they also examine the neglect of attenuating optical depths in Eq. (B2). Calibration offsets should be negligible; contributions to the intensity from gas emissions, and effects from source variability should be also be negligible. Grain evaporation and ice recondensation would affect both the number density n, the cross-section σ, and

the optical properties (so Eq. B2 would not be valid); the overall effect is difficult to quantify, but Thomas and Keller argue that it is unlikely that either evaporation or recondensation could dominate scattering. They conclude that the spatial dependence of $\langle \nu \cos \chi \rangle Z$ determines the behavior of the right-hand side of Eq. (B10).

Thomas and Keller then make several geometric observations concerning Eq. (B10) and the extent to which the behavior of the term Z, measured by Giotto HMC, puts a constraint on the source enclosed in the Gaussian volume:

(1) Referring to their Section 4, they note as a preliminary step that in the region near the tangent point to which the line-of-sight integral in Eq. (B8) is restricted, the surface normal is almost entirely in the image plane (and the Gaussian volume is locally approximately cylindrical). If we decompose the velocity into a component parallel to the image plane, $\mathbf{v}_{\parallel} = \nu_{x'}\mathbf{e}_{x'} + \nu_{y'}\mathbf{e}_{y'}$, and a component perpendicular to the image plane $\mathbf{v}_{\perp} = \nu_{z'}\mathbf{e}_{z'}$, then $\nu \cos \chi$ is approximately determined by the component of velocity in the image plane: $\nu \cos \chi \approx \mathbf{v}_{\parallel} \cdot (\mathbf{f}_{\Phi'} \times \mathbf{f}_s) r_0/(s\rho)$.

(2) In force-free flow the dust follows a linear trajectory from its ejection point on the nucleus at a constant speed, and $\mathbf{v}_{\parallel}$ remains constant. In this case, they show geometrically that $\cos \chi$ increases to a constant monotonically as ρ increases. In this case if dust is emitted at the surface in some direction off the surface normal, $\cos \chi$ will increase to its asymptotic value as ρ increases, so Z must decrease with ρ if the enclosed source is constant. To the contrary, Z is observed to increase. Therefore either non-force-free flow effects, and/or extra sources in the Gaussian volume, overwhelm the force-free behavior, and account for the observed dependence of Z on ρ.

(3) They consider non-force-free flow:

(3a) In general, ν is expected to increase with ρ near the surface. If the trajectory is straight, and the enclosed source constant, then Z must decrease with ρ; again this is opposite observations. Therefore either curved flow trajectories, and/or extra sources in the Gaussian volume, overwhelm the effect of ν increasing with respect to ρ.

(3b) They consider acceleration which changes the direction of the flow. If dust is blown (tangentially) completely around the nucleus near the surface, it could exit the Gaussian volume and reenter, yielding a sign change in $\cos \chi$, and reduce $\langle \cos \chi \rangle$. If farther from the surface dust is not blown completely around the nucleus, $\langle \cos \chi \rangle$ will be larger, and the quantity Z will be reduced from the near-surface values if the enclosed source is constant.

They also consider a flow which is curved near the surface, but eventually becomes straight (force-free). Temporarily fix ν, and recall that $\nu \cos \chi$ is determined primarily by the component $\mathbf{v}_{\parallel}$. Suppose the direction of $\mathbf{v}_{\parallel}$ curves near the surface. Passage from curved flow to the asymptotic straight trajectory will be associated with an increase in $\cos \chi$ with ρ, as in case (2). With ν fixed, a decreasing value of the magnitude $|\mathbf{v}_{\parallel}|$ corresponds to curvature of the total velocity out of the image plane, and contributes to a decrease in $\cos \chi$ with ρ. Conversely curvature into the image plane will contribute to an increase in $\cos \chi$ with ρ. Finally, any strong curvature in flow should be associated with speed ν increasing with ρ, as in case (3a). Thomas and Keller argue that the acceleration effects which increase $\langle \nu \cos \chi \rangle$ with ρ should offset (or dominate) effects which decrease $\langle \nu \cos \chi \rangle$ with ρ. Thus again if the enclosed sources are constant, Z would be constant (or decrease) with ρ, opposite observation. Therefore only extra sources in the Gaussian volume can account for the behavior of Z, implying an extended source about the nucleus surface, such that the total enclosed source increases with ρ.

It is expected grains flowing away from the nucleus will fragment due to acceleration and heating stresses. Fragmentation will increase the number density n, and decrease the cross section σ, so in principle the observed intensity could be increased or decreased. Since the arguments summarized above rule out all other possible explanations, Thomas and Keller argue grain fragmentation in the outflow must account for the effective increase in Z with ρ. Using a simple single scattering approximation with optical depths neglected, they calculate a scale height of 15–20 km for fragmentation, and that a rate of at least 2.7 daughters per parent particle would be required to account for the observed dependence of Z on ρ.

ACKNOWLEDGMENTS

This work was supported by NSF Grant AST-9015928 and by NASA Grant NAGW 1366. Acknowledgments are also made to the University of Michigan and to the National Center for Atmospheric Research sponsored by NSF for the computing time used in this research.

REFERENCES

ADAMS, C. N., AND G. W. KATTAWAR 1978. Radiative transfer in spherical shell atmospheres. I. Rayleigh scattering. *Icarus* **35,** 139–151.

CHICK, K. M., AND T. I. GOMBOSI 1992 (Paper I). Multiple scattering of light in a spherical cometary atmosphere with an axisymmetric dust jet. *Icarus* **98,** 179–194.

DIVINE, N., H. FECHTIG, T. I. GOMBOSI, M. S. HANNER, H. U. KELLER, S. M. LARSON, D. A. MENDIS, R. L. NEWBURN JR., R. REINHARD, Z. SEKANINA, AND D. K. YEOMANS 1986. The comet Halley dust and gas environment. *Space Sci. Rev.* **43,** 1–104.

DOLLFUS, A. 1989. Polarimetry of grains in the coma of P/Halley. II. Interpretation. *Astron. Astrophys.* **213,** 469–478.

DOLLFUS, A., AND J. L. SUCHAIL 1987. Polarimetry of grains in the coma of P/Halley. *Astron. Astrophys.* **187,** 669–688.

EATON, N. S. M. SCARROTT, AND R. F. WARREN-SMITH 1988. Polarization images of the inner regions of comet Halley. *Icarus* **76,** 270–278.

EATON, N., S. M. SCARROTT, AND R. D. WOLSTENSCROFT 1991. Polarization studies of comet Okazaki-Levy-Rudenko. *Mon. Not. R. Astron. Soc.* **250,** 654–656.

EDDINGTON, A. S. 1910. The envelopes of comet Morehouse (1908c). *Mon. Not. R. Astron. Soc.* **70,** 442–458.

GOMBOSI, T. I., A. F. NAGY, T. E. CRAVENS 1986. Dust and neutral gas modeling of the inner atmospheres of comets. *Rev. Geophys.* **24,** 667–700.

HANNER, M. S., AND H. CAMPINS 1986. Thermal emission from the dust coma of comet Bowell and a model for the grains. *Icarus* **67,** 51–62.

HELLMICH, R., AND H. U. KELLER 1981. On the visibility of nuclei of dusty comets. *Icarus* **47,** 325–332.

HUEBNER, W. F., W. A. DELAMERE, H. J. REITSEMA, H. U. KELLER, K. WILHELM, F. L. WHIPPLE, AND H. U. SCHMIDT 1986. Dust-gas interaction deduced from Halley Multicolor Camera observations. In *Symposium on the exploration of Halley's comet,* (B. Battrick, E. J. Rolfe, and R. Reinhard, Eds.), Vol. 2, p. 363. ESA-SP 250 ESA, Paris.

HUEBNER, W. F., D. C. BOICE, H. J. REITSEMA, AND W. A. DELAMERE 1988. A model for intensity profiles of dust jets near the nucleus of comet Halley. *Icarus* **76,** 78–88.

KATTAWAR, G. W., AND C. N. ADAMS 1978. Radiative transfer in spherical shell atmospheres. II. Asymmetric phase functions. *Icarus* **35,** 436–449.

KELLER, H. U., W. A. DELAMERE, W. F. HUEBNER, H. J. REITSEMA, H. U. SCHMIDT, F. L. WHIPPLE, K. WILHELM, W. CURDT, R.

KRAMM, N. THOMAS, C. ARPIGNY, C. BARBIERI, R. M. BONNET, S. CAZES, M. CORADINI, C. B. COSMOVICI, D. W. HUGHES, C. JAMAR, D. MALAISE, K. SCHMIDT, W. K. H. SCHMIDT, AND P. SEIGE 1987. Comet P/Halley's nucleus and its activity. *Astron. Astrophys.* **187,** 807–823.

KELLER, H. U., M. L. MARCONI, AND N. THOMAS 1990. Hydrodynamic implications of particle fragmentation near cometary nuclei. *Astron. Astrophys.* **227,** L1–L4.

KELLER, H. U., AND N. THOMAS 1989. Evidence for near-surface breezes on comet P/Halley. *Astron. Astrophys.* **226,** L9–L12.

KITAMURA, Y. 1986. Axisymmetric dusty gas jet in the inner coma of a comet. *Icarus,* **66,** 241–257.

KITAMURA, Y. 1990. A numerical study of the interaction between two cometary jets: A possibility of shock formation in cometary atmospheres. *Icarus* **86,** 455–475.

KONNO, I., W. F. HUEBNER, AND D. C. BOICE 1992. A model of dust fragmentation in near-nucleus jet-like features in comet P/Halley. *Icarus,* in press.

KÖRÖSMEZEY, A., AND T. I. GOMBOSI 1990. A time-dependent dusty gas dynamic model of axisymmetric cometary jets. *Icarus* **84,** 118–153.

LEWIS, E. E., AND W. F. MILLER, JR. 1984. *Computational Methods of Neutron Transport.* Wiley, New York.

METZ, K., AND R. HAEFNER 1987. Circular polarization near the nucleus of Comet P/Halley. *Astron. Astrophys.* **187,** 539–542.

MOKHNACH, D. O. 1938. On the physical processes in the head of a comet. *Ann. Leningrad State Univ.,* Astr. series issue 4.

MOKHNACH, D. O. 1958a. The nonstationary distribution of apparent density in comets. *Soviet Astron AJ* **2,** 560–572.

MOKHNACH, D. O. 1958b. The general case of stationary visual density distribution in the head of a comet which exhibits constant isotropic emission. *Soviet Phys Doklady* **3,** 492–494.

MUKAI, T., S. MUKAI, AND S. KIKUCHI 1987. Complex refractive index of grain material deduced from the visible polarimetry of comet P/Halley. *Astron. Astrophys.* **187,** 650–652.

MUKAI, S., T. MUKAI, AND S. KIKUCHI 1991. Scattering properties of cometary dust based on polarimetric data. In *Origin and Evolution of Interplanetary Dust,* (A. C. Levasseur-Regourd and H. Hasegawa, Eds.), pp. 249–252, Kluwer, Japan.

REITSEMA, H. J., W. A. DELAMERE, A. R. WILLIAMS, D. C. BOICE, AND W. F. HUEBNER 1989. Dust distribution in the inner coma of Comet Halley: Comparison with models. *Icarus* **81,** 31–40.

RENARD, J. B., A. C. LEVASSEUR-REGOURD, AND A. DOLLFUS 1992. Polarimetric CCD imaging of comet Levy (1990c). *Ann. Geophysicae* **10,** 288–292.

RICKMAN, H., L. KAMÉL, C. FROESCHLÉ, AND M. C. FESTOU 1991. Nongravitational effects and the aging of periodic comets. *Astron. J.* **102,** 1446–1463.

SEKANINA, Z. 1987. Anisotropic emission from comets: Fans versus jets. I. Concepts and modeling. In *Symposium on the Diversity and Similarity of Comets,* pp. 315–322. European Space Agency, Noordwijk, Neth.

SEKANINA, Z. 1990. Gas and dust emission from comets and life spans of active areas on their rotating nuclei. *Astron. J.* **100,** 1293–1314.

SEN, A. K., U. C. JOSHI, M. R. DESHPANDE, AND C. DEBI PRASAD 1990. Imaging polarimetry of Comet P/Halley. *Icarus* **86,** 248–256.

SZEGÖ, K., I. TÓTH, Z., SZATMÁRY, B. A. SMITH, A. KONDOR, AND E. MERÉNYI 1988. *Dust Photometry in the Near Nucleus Region of Comet Halley.* KFKI-1988-33/C.

THOMAS, N., AND H. U. KELLER 1987. Comet P/Halley's near nucleus jet activity. In *Symposium on the Diversity and Similarity of Comets.* ESA SP-278, pp. 337–342.

THOMAS, N., AND H. U. KELLER 1990. Interpretation of the inner coma observations of comet P/Halley by the Halley Multicolor Camera. *Ann. Geophys.* **8,** 147–166.

THOMAS, N., AND H. U. KELLER 1991. Comet P/Halley's dust production rate at Giotto encounter derived from Halley Multicolor Camera observations. *Astron. Astrophys.* **249,** 258–268.

WALLACE, L. V., AND F. D. MILLER 1958. Isophote configurations for model comets. *Astron. J.* **63,** 213–219.

WEAVER, H. A., M. F. A'HEARN, P. D. FELDMAN, C. ARPIGNY, W. A. BAUM, J. C. BRANDT, R. M. LIGHT, AND L. A. WESTPHAL 1992. Inner coma imaging of comet Levy (1990c) with the Hubble Space Telescope. *Icarus* **97,** 85–98.